Advanced Composites and Hybrid Materials (2026) 9:95
https://doi.org/10.1007/s42114-026-01649-2

RESEARCH

Achieving super wear resistance in additively manufactured eutectic high-entropy alloys via self-hardening design at intermediate temperatures

Yixuan Sun[1] · Chunjin Wang[1] · Rui Gao[1] · Chuanxi Ren[1,2] · Changning Bai[1] · Dingding Xiang[3] · Chi Fai Cheung[1] · Zibin Chen[1,2]

Received: 9 October 2025 / Revised: 13 January 2026 / Accepted: 15 January 2026

Abstract
Interfacial degradation, oxidative damage, and fatigue cracking pose persistent challenges to structural alloys operating in the intermediate-temperature regime (400–600 °C), often resulting in accelerated wear and premature failure. To address this, we design a multicomponent Ti-containing eutectic high-entropy alloy (EHEA) via additive manufacturing (AM) and targeted Ti alloying to engineer a thermally stable, refined microstructure tailored for enhanced tribological performance. The resulting alloy achieves an ultralow wear rate of 6.20×10^{-5} mm³/N·m at 600 °C—approximately 86% lower than that of conventional Ni-based superalloys. Microstructural analyses reveal that rapid AM solidification produces ultrafine equiaxed grains with >90% high-angle grain boundaries, stabilized by Ni segregation and contributing to robust Hall–Petch strengthening. Ti addition not only stabilizes the B2 phase (~87 vol%) but also promotes the selective formation of dense Al_2O_3/Cr_2O_3 oxide scales, which suppress oxidative wear. Further friction triggers the in-situ formation of Ni-rich hexagonal close-packed (HCP) nanoprecipitates, which accommodate strain and provide in-situ self-hardening. The multi-structural system enables the alloy to overcome the temperature–wear trade-off typically observed in conventional HEAs at intermediate temperatures. This study establishes a new alloy design strategy that integrates AM-enabled grain boundary engineering with element-specific oxidation control to realize wear-resistant structural materials for intermediate-temperature applications.

Keywords Eutectic high entropy alloy · Alloy design · Additive manufacturing · Wear resistance · Oxidation resistance · Self-hardening

1 Introduction

Wear-induced interfacial failure at intermediate temperatures (400–600 °C) poses a significant challenge to aerospace turbines, nuclear reactors, and advanced manufacturing systems, contributing to global economic losses exceeding $500 billion annually [1, 2]. Conventional Ni-/Co-based superalloys exhibit excellent mechanical properties below 500 °C but suffer from severe wear rate escalation (> 10^{-4} mm³/N·m) above 600 °C due to brittle oxide scale formation [2]. Eutectic high-entropy alloys (EHEAs), particularly $AlCoCrFeNi_{2.1}$, have emerged as promising alternatives, offering an exceptional strength–ductility balance (> 1 GPa strength, > 15% elongation) at room temperature, facilitated by coherent FCC/B2 interfaces with Kurdjumov-Sachs (K-S) orientation relationships [3, 4].

✉ Chunjin Wang
chunjin.wang@polyu.edu.hk

✉ Zibin Chen
zi-bin.chen@polyu.edu.hk

[1] State Key Laboratory of Ultra-Precision Machining Technology, Department of Industrial and Systems Engineering, The Hong Kong Polytechnic University, Kowloon, Hong Kong, China

[2] Research Institute for Advanced Manufacturing, Department of Industrial and Systems Engineering, The Hong Kong Polytechnic University, Hong Kong, China

[3] School of Mechanical Engineering and Automation, Northeastern University, Shenyang 110819, China

Published online: 02 February 2026

However, above 500 °C, interfacial degradation and lamellar coarsening lead to strength loss and embrittlement [5, 6]. While prior studies report nanocrystalline-amorphous oxide layers with superior wear resistance at room temperature and strength recovery above 800 °C [6], the intermediate-temperature regime remains problematic, where thermal softening, brittle oxide formation, and cyclic loading exacerbate wear and delamination [7, 8].

Stabilizing grain structures at intermediate temperatures represents a crucial aspect, as grain boundaries tend to migrate and coarsen with increasing temperature, potentially embrittling the material [9]. To address these challenges, microstructural stabilization strategies—such as solute drag, Zener pinning, and Gibbs adsorption—have been explored. Solute drag, achieved via dopants like Si in FeNiCrAlCuSi HEA, exploits segregation at grain boundaries to retard migration, reducing wear rates by ~ 40% [10]. Similar effects are observed in V- and Cr-enriched HEAs processed by hot-isostatic pressing, where solute drag forces were intensified to refine grains to < 2 μm, significantly increasing hardness [11]. Zener pinning, utilizing finely dispersed precipitates to physically impede grain boundary movements, offers an alternative stabilization mechanism. Enabled by σ-phase nanoprecipitates (50–100 nm) in aged AlxCoCrFeNi systems, robust interfacial networks were formed to suppress grain growth at 600 °C, reducing wear mass loss from 9.2 × 10^{-5} to 6.4 × 10^{-5} $mm^3/N·m$ [12]. Additionally, EHEAs exhibit nanoscale coherent $L1_2$ precipitates within their B2 matrices, further leveraging Zener-like drag effects to resist grain coarsening effectively [13]. Finally, Gibbs adsorption stabilizes grain boundaries by reducing boundary energy through elemental segregation, thus diminishing migration kinetics [14]. For example, the Gibbs adsorption demonstrated in CoCrCuFeTi HEAs annealed at 650 °C promotes Cr/Ti segregation at boundaries, lowering grain boundary free energy by ~ 10% and reducing friction coefficients from 0.62 to 0.45 [15]. These targeted stabilization methods effectively mitigate grain boundary migration and coarsening, enhancing structural stability, which improves subsurface performance under sliding conditions, leading to greater load-bearing and load-transferring capacity through more stable subsurface structures [16]. However, conventional processing routes often face inherent limitations in achieving optimal microstructural stability. In particular, as-cast EHEAs are prone to rapid microstructural degradation, where lamellae coarsen rapidly—a simple 500 °C/2 h exposure doubles the lamellar width and markedly softens the alloy, further undermining wear resistance [17, 18]. To overcome these processing-related constraints, Additive manufacturing (AM) offers a compelling solution by enabling rapid solidification (10^7–10^8 K/s), solute trapping, and refined grains, thereby improving thermal stability [19–21]. The extreme cooling rates achievable through AM facilitate the retention of supersaturated solid solutions and suppress the formation of deleterious phases that might otherwise compromise grain boundary integrity [22]. Furthermore, when coupled with strategic Ti alloying, which stabilizes the B2 phase and enhances solid-solution strengthening, AM-processed EHEAs can synergistically combine rapid solidification benefits with compositional optimization, resulting in enhanced load-bearing and load-transferring capacity through more stable subsurface structures [5, 23].

Oxidation resistance is also critical for wear performance at intermediate temperatures. Among multicomponent EHEA systems, Al and Cr are foundational elements due to their ability to form thermally stable α-Al_2O_3 and Cr_2O_3 phases that act as effective diffusion barriers [24]. However, Fe- and Ni-derived oxides (Fe_2O_3, $NiCr_2O_4$) are mechanically soft and prone to repeated fracture under cyclic sliding, forming unstable, non-protective layers that accelerate material degradation [24]. This challenge is particularly acute in EHEAs, which often undergo non-selective oxidation at 400–600 °C, forming mechanically mixed oxides (Al_2O_3/Cr_2O_3/Fe_3O_4) with poor adhesion and spallation tendencies [25]. Ti-containing systems, on the other hand, offer a promising solution, as Ti^{4+} substitution for Al^{3+} in Al_2O_3 generates additional oxygen vacancies that enhance cation outward diffusion, promoting rapid formation of dense, adherent Al_2O_3-rich scales [26]. Compared to undoped alloys, Ti-containing EHEAs exhibit dramatically reduced oxide spallation, with oxidation rates lowered by up to two orders of magnitude [27, 28]. The improved compositional uniformity and strain tolerance of Ti-modified oxide layers further mitigate crack formation, enhancing structural integrity under sliding conditions [26].

In this work, we develop a multicomponent Ti-modified $AlCoCrFeNi_{2.1}$ EHEA via AM to overcome the wear-induced degradation in the intermediate-temperature range (400–600 °C). We systematically evaluated the AM-fabricated Ti-modified EHEA variants through microstructural characterization and dry sliding wear experiments at 400 °C and 600 °C. The alloy exhibits a refined B2-dominated microstructure (~ 3.3 μm grain size, > 90% HAGBs). Wear testing at 600 °C revealed a low specific wear rate of 6.2 × 10^{-5} $mm^3/N·m$, significantly lower than the EHEA-counterpart of 3.2 × 10^{-4} $mm^3/N·m$. These enhancements are attributed to the synergy of ultrafine microstructures, Ti-stabilized B2 phase retention, in-situ hexagonal close-packed (HCP) precipitation, and the selective formation of dense Al_2O_3/Cr_2O_3 scales under frictional conditions. These findings demonstrate a transition of wear mechanism, from oxidative and fatigue-dominated to mild abrasive and plastic deformation, offering a pathway for designing self-hardening materials for intermediate-temperature applications.

2 Experimental procedures

2.1 Material preparations

Rectangular blocks (35 × 15 × 5 mm) were fabricated on an unheated 316 L stainless-steel substrate using a Laser Engineering Net Shaping (LENS) MR-7 system (Optomec) under argon (< 100 ppm O_2). The equipment schematic is shown in Fig. 1a (yellow/red indicates peak temperature; orange-gray shows solidification). The scanning strategy is illustrated in Fig. 1b. A 2 mm-diameter laser beam with 400 W power was scanned at 6 mm/s to melt each 0.3 mm layer. Successive layers were rotated by 90° to promote an isotropic microstructure. Process parameters were optimized via preliminary trials to achieve ≥ 99.8% theoretical density (Archimedes), with no detectable porosity or surface defects. Gas-atomized pre-alloyed $AlCoCrFeNi_{2.1}$ powder (45–105 µm, > 99.9 wt%) was dry-mixed with high-purity Ti powder (45–105 µm, > 99.9 wt%) in a 3D Turbula blender for two hours to obtain the EHEA-Ti powder mixture (4.68 at% Ti). The printed samples are referred to as AM-EHEA and AM-EHEA-Ti. The equiaxed grain structures of AM-EHEA-Ti, observed from top and side views via EBSD inverse pole figure (IPF) mapping, are shown in Fig. 1b. All LENS-built specimens were wire-cut by electrical discharge machining (EDM) at the same build height to ensure identical thermal histories for subsequent testing (Fig. 1c). Equilibrium phase calculations using Thermo-Calc™ demonstrate that 4.68 at% Ti marks the onset of precipitation phase at 500 °C (Fig. 1d). Final alloy compositions are listed in Table 1.

2.2 Microstructural characterization

Microstructures and elemental distributions were analyzed by (scanning) transmission electron microscopy ((S)TEM) coupled with energy-dispersive X-ray spectroscopy (EDX) on a Talos F200X G2 microscope operated at 200 kV. Electron energy loss spectroscopy (EELS) measurements were performed on a Thermo Fisher Scientific Spectra 300 S/TEM at 300 kV accelerating voltage (E_0=300 kV). STEM-HAADF imaging was used to guide positioning and locate the oxide layer/substrate transition regions beneath wear tracks, with priority given to areas showing uniform thickness and minimal voids for spectrum imaging (SI) or line scan acquisition. The electron optical conditions were: convergence semi-angle = 29.0 mrad and collection semi-angle = 33.6 mrad. Cross-sectional specimens were prepared by focused ion beam (FIB) and subjected to final thinning using 2–5 kV low-voltage ion cleaning to minimize surface damage and redeposition artifacts. Plan-view TEM specimens were mechanically polished to controlled depth, then thinned to ~ 25 µm by bilateral polishing, with final electron transparency achieved via a Gatan 695 precision ion polishing system. Grain orientation and phase mapping were obtained by electron backscatter diffraction (EBSD) analyses in an Apreo 2 S field-emission scanning electron microscope (SEM) (Oxford C Symmetry S2 detector) at 20 kV. Samples were ground by #2000-grit SiC sandpaper, finished with SiO_2 suspension (average size 0.02 µm), and electrolytically polished in 10% $HClO_4$ and 90% ethanol solution at room temperature. TEM analyses for intermediate temperature samples were performed on unstrained upper shoulder

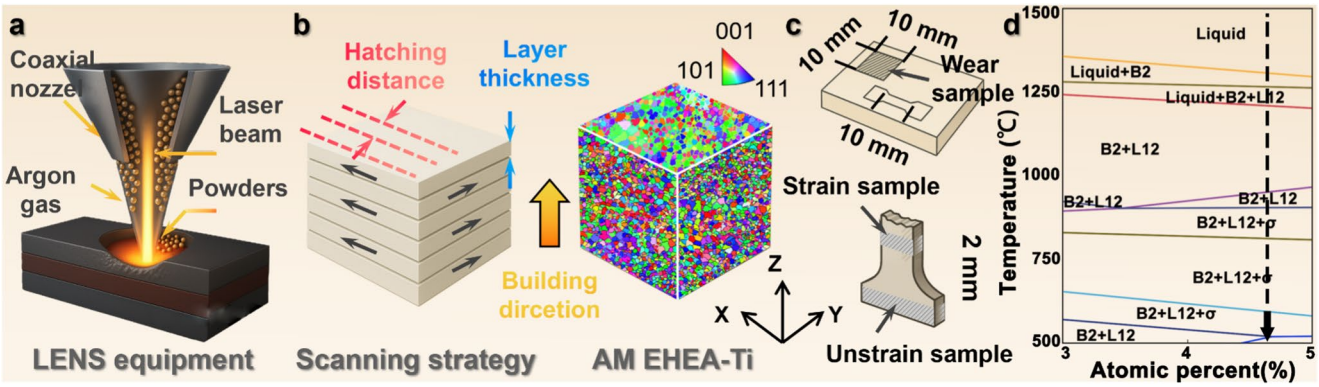

Fig. 1 LENS fabrication schematic and equilibrium phase calculation. (**a**) The LENS system setup shows powder feeding and laser scanning. (**b**) The scanning strategy in the experiment and the IPF structure of AM-EHEA-Ti from cross-section along the building direction (Z) and top view perpendicular (X-Y) to the building direction. (**c**) Sample extraction locations by EDM for microstructural and mechanical tests. (**d**) The calculated equilibrium phase diagram as a function of Ti content extracted from the ThermoCalc™ software

Table 1 Experimental composition (by EDS) of EHEA and EHEA-Ti alloys via AM, respectively

Sample	Al (wt%)	Cr (wt%)	Fe (wt%)	Co (wt%)	Ni (wt%)	Ti (wt%)
AM-EHEA	6.31 ± 0.77	17.80 ± 0.23	18.47 ± 0.32	19.50 ± 0.48	37.13 ± 0.79	/
AM-EHEA-Ti	7.57 ± 0.38	15.03 ± 0.58	16.49 ± 0.33	17.18 ± 0.16	34.85 ± 0.82	4.33 ± 0.66

regions away from deformation zones, as shown in Fig. 1c. Specimens tested along the building direction corresponded to the Z-axis of LENS-fabricated samples, perpendicular to the deposition plane.

2.3 Mechanical measurements

Microhardness measurements were carried out on polished specimens with surfaces parallel to the build (Z) direction using a ZD-HVZHT-30 tester. A 500 gf load was applied for 10 s at each indentation, with a 3-minute holding time at the target temperature, and at least three measurements were taken per sample to ensure consistency. Wear behavior was evaluated following ASTM G99-17 using 10 × 10 mm disks of EHEA-Ti and 6 mm-diameter Si_3N_4 balls on an Anton-Paar THT tribometer. Prior to testing, disk surfaces were ground sequentially by #3000-grit SiC sandpaper, then polished with SiO_2 suspension (average size 0.02 μm) to achieve Ra < 5 nm, Rq < 10 nm, and Rz < 1 μm. Tests were conducted in dry air at room temperature, 400 °C, and 600 °C under 5 N normal load, 0.1 m/s sliding velocity, and 500 m total sliding distance. Heating followed the same 10 °C/min rate as tensile tests to match thermal history, and unstrained tensile specimens served as wear references at the upper shoulder (Fig. 1c).

Wear tracks were profiled with a Zygo NEXVIEW white-light interferometer to obtain the wear area (A). Wear volume, V, was calculated as $V = A \cdot \pi d$, where $d = 60$ mm is the track diameter. The specific wear rate, W (mm³/N·m), was determined by $W = V/FL$, where F is the normal load, and L is the sliding distance. Each test was performed in triplicate, and the mean wear rate and coefficient of friction (COF), together with standard deviations, were reported.

3 Results

3.1 Tribological performances of multicomponent Ti-containing EHEAs at intermediate temperatures

Tribologically (Fig. 2), the AM-EHEA-Ti induces a counterintuitive inverse temperature-wear effect. At 400 °C (Fig. 2a), the COF curves of both Ti-containing and Ti-free AM-EHEAs exhibit similar trends and comparable values. However, at 600 °C, AM-EHEA-Ti demonstrates markedly different COF behavior compared to AM-EHEA. While the latter exhibits continuously rising COF, the former reaches a stable, significantly lower steady-state COF after the initial stage. The statistical analysis of average COF values reveals distinct temperature-dependent trends for AM-EHEA and AM-EHEA-Ti (Fig. 2b). AM-EHEA exhibits relatively stable friction performance across the temperature range, with COF values of 0.67 ± 0.20 at room temperature, 0.57 at 400 °C, and 0.64 ± 0.06 at 600 °C—indicating minor

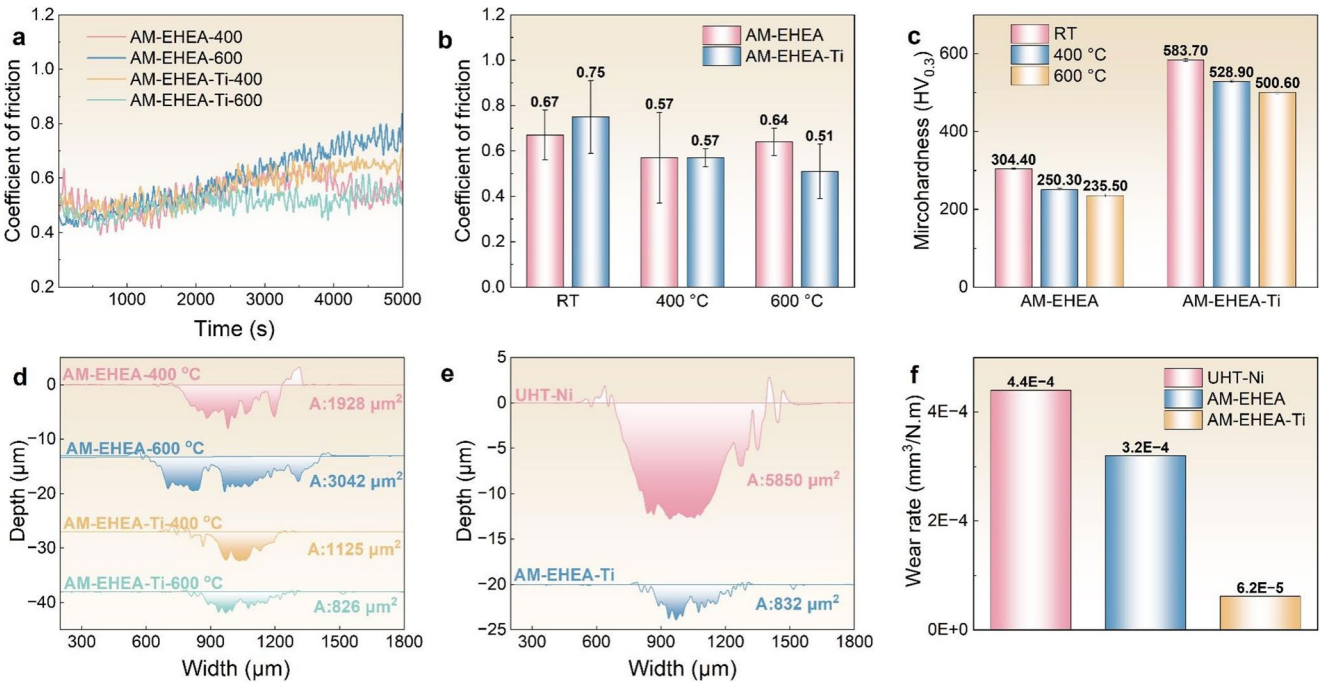

Fig. 2 Tribological performance of AM-EHEA and AM-EHEA-Ti. The COF curves of (**a**) samples under 400 °C and 600 °C. (**b**) The bar chart illustrates the average COF value for all samples in this study. (**c**) The microhardness of the samples at various temperatures. Representative 2D cross-sectional wear track profiles for (**d**) all the samples under 400 °C and 600 °C. (**e**) The wear performance comparison of AM-EHEA-Ti and UHT-Ni alloy samples at 600 °C. (**f**) The wear rate of AM-EHEA-Ti compared with the UHT-Ni samples under 600 °C

fluctuation with temperature. In contrast, AM-EHEA-Ti shows a clear decreasing trend. Starting from a higher COF of 0.75 ± 0.16 at room temperature, its COF gradually drops to ~0.57 at 400 °C—matching AM-EHEA—and further decreases to 0.51 ± 0.11 at 600 °C. Typically, wear rate increases with temperature as materials soften; however, AM-EHEA-Ti exhibits the opposite behavior. The elevated room-temperature COF of AM-EHEA-Ti correlates with its substantially higher hardness (Fig. 2c). At room temperature, AM-EHEA-Ti exhibits a hardness of 583.7 ± 2.7 HV, nearly double that of AM-EHEA (304 ± 4.5 HV). This hardness persists at elevated temperatures: 528.9 ± 3.5 HV versus 250 ± 3 HV at 400 °C, and 500.6 ± 3.3 HV versus 235.5 HV at 600 °C. This inverse temperature dependence indicates that while AM-EHEA-Ti initially exhibits higher friction, it progressively outperforms AM-EHEA at elevated temperatures, ultimately achieving superior tribological performance under intermediate-temperature conditions. The representative wear track cross-section profiles (Fig. 2d) further corroborate these findings. At 400 °C, despite similar COF values, AM-EHEA-Ti exhibits a significantly smaller wear area (1125 μm²) compared to AM-EHEA (1928 μm²). As the temperature increases to 600 °C, the wear behavior diverges more dramatically: the wear area of AM-EHEA further expands to 3042 μm², whereas that of AM-EHEA-Ti decreases markedly to just 826 μm². This substantial reduction in wear area for AM-EHEA-Ti correlates well with its lower COF at this temperature. This discrepancy can be explained by the Vickers hardness measurements (Fig. 2c), which reveal that the wear rate is inversely proportional to hardness. Significantly higher hardness values for the AM samples confirm that the superior wear resistance of AM-EHEA-Ti stems from unique microstructural characteristics induced by the rapid solidification during the AM process.

To benchmark the tribological performance of the AM-EHEA-Ti systems, their wear rates were compared with commercial Ni-based (Ultra-High Temperature Alloy, denoted as UHT-Nickel) reference material. The 2D cross-sectional profiles of wear tracks presented in Fig. 2e highlight the superior wear resistance of AM-EHEA-Ti compared to commercial Ni-based alloys. Specifically, the Ni-based alloy exhibits a large wear area of 5850 μm², whereas AM-EHEA-Ti shows a dramatically reduced wear area of only 823 μm², demonstrating the remarkable effectiveness of AM-EHEA-Ti in minimizing material loss during wear. To gain further insight into the wear interaction, the morphology and area of the wear scars on the Si_3N_4 counterface balls and the calculated wear scar areas were examined in SI Fig. S5. Against AM-EHEA, the scar area increased markedly at 600 °C (0.484 mm²), indicating severe interfacial damage. In contrast, the scar areas against AM-EHEA-Ti were lower at 400 °C (0.374 mm²) and 600 °C (0.390 mm²) compared to room temperature. This consistent reduction in counterface wear aligns with the superior wear resistance of AM-EHEA-Ti, suggesting a transition to a milder abrasive regime facilitated by its stable protective oxide layer and reduced material transfer. AM-EHEA-Ti achieves an unprecedented wear rate of 6.20×10^{-5} mm³/N·m, representing an 86% reduction compared to commercial UHT-Ni, 73% reduction compared to AM-EHEA. This great improvement in wear resistance, combined with maintained intermediate-temperature structural integrity, positions AM-EHEA-Ti as a superior alternative to conventional Ni-based superalloys for demanding tribological applications.

3.2 Microstructures of the as-fabricated multicomponent Ti-containing EHEAs

Figure 3 presents the cross-sectional EBSD IPF maps and phase maps of AM-EHEA and AM-EHEA-Ti samples prior to deformation at room temperature. AM-EHEA maintains a typical lamellar eutectic microstructure with FCC and B2 phases. The B2 phase content was measured at 30.6% for AM-EHEA. For Ti-containing alloys (Fig. 3a), notably, Ti addition dramatically increases the 86.8% B2 phase content in AM-EHEA-Ti alloys [29], directly contributing to the superior hardness observed in Fig. 2c. The microstructures with HAGBs and Low Angle Grain Boundaries (LAGBs) of Ti-free samples are shown in Fig. 3b. HAGBs play a crucial role in enhancing mechanical properties through effectively impeding grain boundary movement, contributing to grain structure strengthening and stability, promoting enhanced intermediate-temperature tribological performances [7]. This higher B2 fraction results from rapid solidification kinetics that promote solute trapping and suppress elemental diffusion, thereby stabilizing Ti-rich B2 domains and transforming the microstructure into equiaxed grains [30]. The AM-processed alloy exhibits a significantly higher proportion of HAGBs (91.2%, Fig. 3b) compared with the as-cast sample (66.7%, Fig. S3), with a normal distribution and a refined grain size of 3.3 ± 0.8 μm. This combined effect of enhanced constitutional supercooling disrupts epitaxial growth, and repeated thermal cycling tailors the microstructure [31] toward increased B2 phase content and refined, isotropic grains, distinguishing AM-fabricated EHEA-Ti from cast counterparts. To further corroborate the phase identification and quantify the elemental partitioning, STEM-EDS mapping and quantitative analysis were conducted on the AM-EHEA-Ti sample, as presented in Fig. 3c; Table 2 confirms a clear compositional distribution: the B2 phase is predominantly enriched in Al and Ti, while the FCC phase is primarily composed of Ni, Co, Cr, and Fe. This direct chemical evidence solidifies the EBSD-based phase mapping and explicitly links Ti addition to the stabilization and

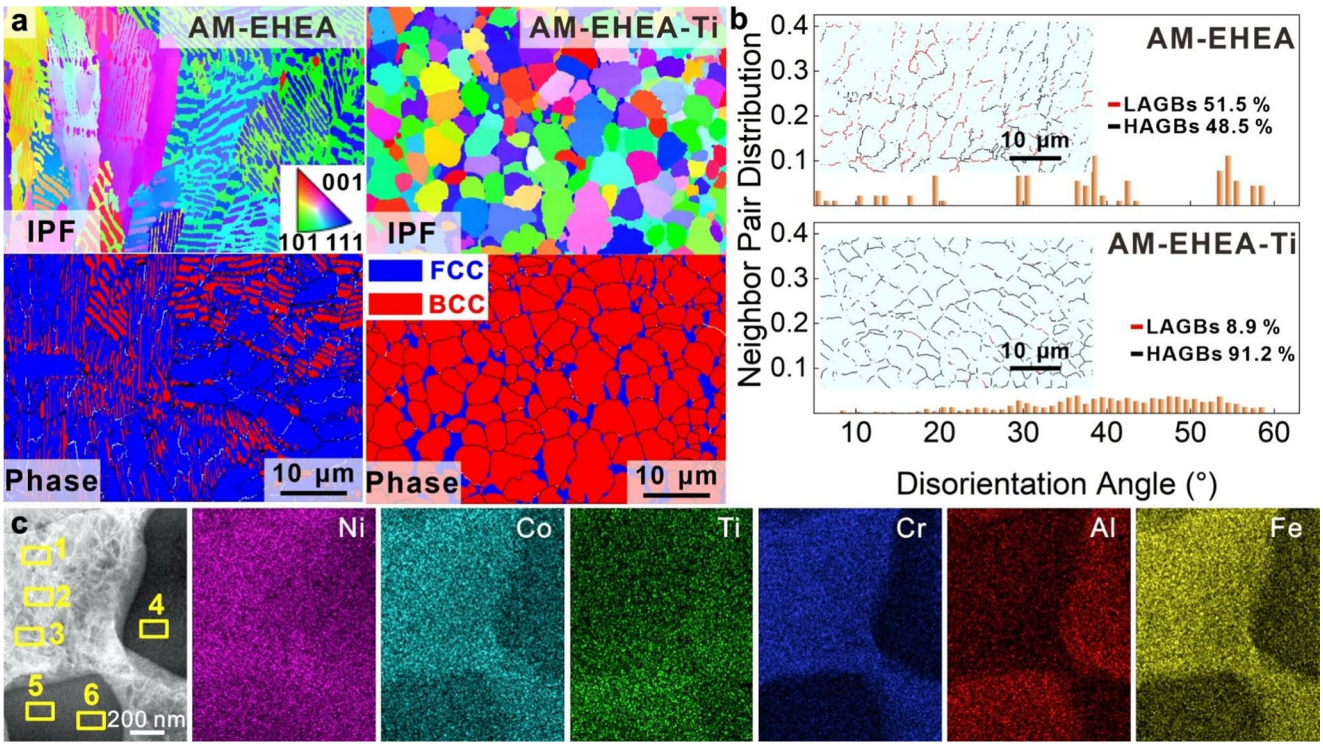

Fig. 3 EBSD characterization of as-fabricated samples along the building direction (Z direction). (**a**) IPF maps and phase maps for AM-EHEA and AM-EHEA-Ti, (**b**) corresponding grain boundary misorientation distribution for AM-EHEA and AM-EHEA-Ti, showing HAGB (≥15°) and LAGB (2°–15°) fractions. (**c**) STEM-EDS mapping showing the element distribution in the AM-EHEA-Ti sample

Table 2 STEM-EDS mapping analysis from Fig. 3c, at%

Phase	Area	Al	Ti	Cr	Fe	Co	Ni
FCC	Area 1	6.77	3.99	20.02	20.68	17.08	31.44
	Area 2	7.21	3.93	20.13	20.77	16.98	30.97
	Area 3	5.50	4.19	20.08	21.04	17.20	31.99
	Mean	6.72 ± 0.90	4.13 ± 0.16	20.40 ± 0.96	20.47 ± 1.21	16.80 ± 0.48	31.48 ± 0.66
B2	Area 4	17.90	7.05	11.08	17.60	15.40	30.97
	Area 5	19.02	9.05	9.97	11.07	14.49	36.40
	Area 6	14.88	9.35	10.91	15.65	14.92	34.30
	Mean	17.3 ± 3.3	8.5 ± 2.3	10.6 ± 5.03	15.4 ± 2.99	15.0 ± 0.37	33.2 ± 2.62

dominance of the B2 phase. AM-EHEA-Ti yields microstructural advantages that directly contribute to enhanced tribological properties: a unique grain boundary architecture characterized by 91.2% HAGBs with a Gaussian-type misorientation distribution, triple the HAGB density of cast counterparts (33.3%). This optimized network arises from the synergistic action of AM's rapid solidification kinetics—marked by high cooling rates, steep thermal gradients, and cyclic thermal reheating—which, together with Ti-induced elevation of the growth-restriction factor (Q) that broadens the constitutional-supercooling zone (ΔT_{CS}) ahead of the solid–liquid interface, drives prolific heterogeneous nucleation and equiaxed grain refinement (flower-shaped grain by cast in Fig. S3), yielding ultrafine grains of 3.3 ± 0.8 μm [31]. Concurrently, Ti acts as a potent B2 stabilizer by increasing the valence electron concentration (VEC) into the BCC-favorable regime and boosting mixing entropy. This drives Ti atoms to preferentially occupy BCC lattice sites, causing lattice expansion, internal stress, and net reduction in Gibbs free energy of mixing (ΔG_{mix})—all of which amplify the thermodynamic driving force for BCC to B2 transformation. As a result, the ordered B2 fraction rises from 30.6% in AM-EHEA to 86.8% in AM-EHEA-Ti [32]. The resultant microstructure combines three critical advantages: a dense HAGB network that obstructs grain boundary motion while enabling stress redistribution through isotropic boundary arrangement, ultrafine equiaxed grains that enhance Hall-Petch strengthening [33] and inhibit grain boundary sliding, and B2 phase dominance that provides intrinsic lattice strengthening. This microstructural triad,

unobtainable through conventional processing, directly contributes to the anomalous wear resistance, establishing a new paradigm for designing intermediate-temperature structural alloys where rapid solidification enables atomic-scale solute control while chemical alloying tailors phase stability.

The AM-EHEA-Ti alloying is demonstrated in Fig. 4. The high-angle annular darkfield (HAADF)-STEM analysis of AM-EHEA-Ti (Fig. 4a) revealed equiaxed microstructures with a mean grain diameter of approximately 3.3 μm (range: 0.4–9.8 μm). The selected area diffraction pattern (SADP) along [001] confirmed the B2 matrix structure with characteristic superlattice spots. The enlarged HAADF shows the dual-phase structure (Fig. 4b) with elemental mapping revealing distinct Ni-rich zones at phase boundaries (Fig. 4b_1), consistent with GB segregation patterns in AM-fabricated materials. Based on the Miedema model [34], the segregation enthalpy of Ti in a Ni matrix is approximately − 24.9 kJ/mol [35], indicating a strong driving force for Ti to migrate toward grain boundaries. However, in the Ti-Al-Ni system, Ti and Al exhibit the lowest bonding enthalpy of ~−32 kJ/mol compared to other pairs, favoring their mutual incorporation into the grain interior [36], leading to Ti-Al enriched regions as shown in Figs. 4b_2-b_3. In contrast, Ni, with a smaller atomic radius (1.24 Å, vs. 1.43 Å for Ti and Al) and weaker bonding tendency (Ti-Ni: −10 kJ/mol) [37], is energetically less compatible with the matrix. During AM, the high cooling rates and suppressed atomic diffusion promote solute trapping, preventing Ni redistribution and enhancing segregation. HRTEM analysis (Fig. 4c) revealed phase boundaries with deteriorated orientation relationships and increased misfit dislocations, corresponding to the high proportion of HAGBs observed in EBSD analysis. Figure 4d presents the HRTEM image of the FCC phase enveloping the equiaxed B2 matrix. Correspondingly, Fig. 4d_1 displays the FFT pattern of the FCC matrix, Fig. 4d_2 shows the FFT of the $L1_2$ precipitates, and Fig. 4d_3 presents the inverse FFT (IFFT) of $L1_2$ precipitates region 2, highlighting $L1_2$ precipitates approximately 17.78 nm in diameter. The incorporation of Ti, with a relatively large atomic radius (1.47 Å) compared to the smaller constituent elements in the FCC matrix, such as Co, Cr, and Ni (ranging from 1.24 to 1.38 Å), introduces significant lattice distortion and reduces the solid solution stability. This atomic size mismatch increases the elastic strain energy in the matrix and thereby provides a thermodynamic driving force for the $L1_2$ phase precipitation [38]. Off-axis dark-field TEM images along g = 100 (Fig. 4e) revealed spherical and rod-shaped particles with a diameter of 35.66 ± 5.3 nm, and SADP patterns confirmed B2-type superlattice spots (100). Enlarged HAADF in Fig. 4f with STEM-EDS mapping demonstrated that Cr/Ni-rich $D0_3$-FCC precipitates (Figs. 4f_1-f_2) maintain cube-on-cube orientation relationships with the B2 matrix (Fig. 4f_3): [011] $D0_3$-FCC//[011] B2, [001] B2//[001] $D0_3$-FCC, and ($\bar{2}$ 20) $D0_3$-FCC//($\bar{1}$ 10) B2 [5]. HRTEM and corresponding IFFT analysis (Fig. 4g) confirmed the atomic-level B2/$D0_3$-FCC interface with measured lattice constants of FCC 5.67 Å and B2 2.99 Å.

The AM-EHEA-Ti generates a unique hierarchical microstructure featuring equiaxed B2-dominant grains with optimized HAGBs, nanoscale $L1_2$ and $D0_3$-FCC precipitates that provide effective hardening mechanisms [39]; and controlled Ni-elemental segregation that stabilizes grain boundaries [40]. This multi-scale structural engineering explains the exceptional tribological performance in AM-EHEA-Ti alloys at intermediate temperatures. This multiscale architecture stems from synergy between non-equilibrium kinetics and chemical effects, where rapid solidification traps Ti solutes, which modify interfacial energies to enhance B2 nucleation and grain refinement through constitutional supercooling—a mechanism inaccessible via conventional processing.

3.3 Phase evolution of multicomponent Ti-containing EHEA at intermediate temperatures

Figures 5–6 summarize the pre-deformation phase state and compositional evolution of AM-EHEA-Ti in the intermediate-temperature regime. In the as-built condition (Fig. 4e), rapid solidification produces a fully equiaxed grain structure with nanoscale $D0_3$ dispersed in the B2 matrix and $L1_2$ precipitates in the FCC matrix. Upon heating to 400 °C, Fig. 5a shows that the AM-EHEA-Ti sample keeps equiaxed morphology. Accelerated diffusion causes both $L1_2$ and $D0_3$ phases to dissolve back into the FCC and B2 lattices, respectively (Figs. 5b-c). In the as-printed state, the $L1_2$ phase is kinetically trapped within the FCC matrix due to rapid solidification, existing as a thermodynamically metastable phase. Upon heating to 400 °C, enhanced atomic diffusion, combined with the partial release of residual stresses introduced by AM, promotes the reverse dissolution of the $L1_2$ phase, transforming it back to a disordered FCC solid solution. This transformation is governed by the relatively low ordering driving force in the intermediate temperature regime, particularly in high-entropy multicomponent systems where the thermodynamic potential required for long-range ordering is readily offset by the dominant contributions of configurational entropy and diffusion potential [41]. The elevated temperature provides sufficient atomic mobility (Diffusion coefficient: $D \propto e^{-Q/RT}$) [42] to disrupt the next-nearest neighbor ordering arrangement within the $L1_2$ and $D0_3$ phase. Concurrently, the strong

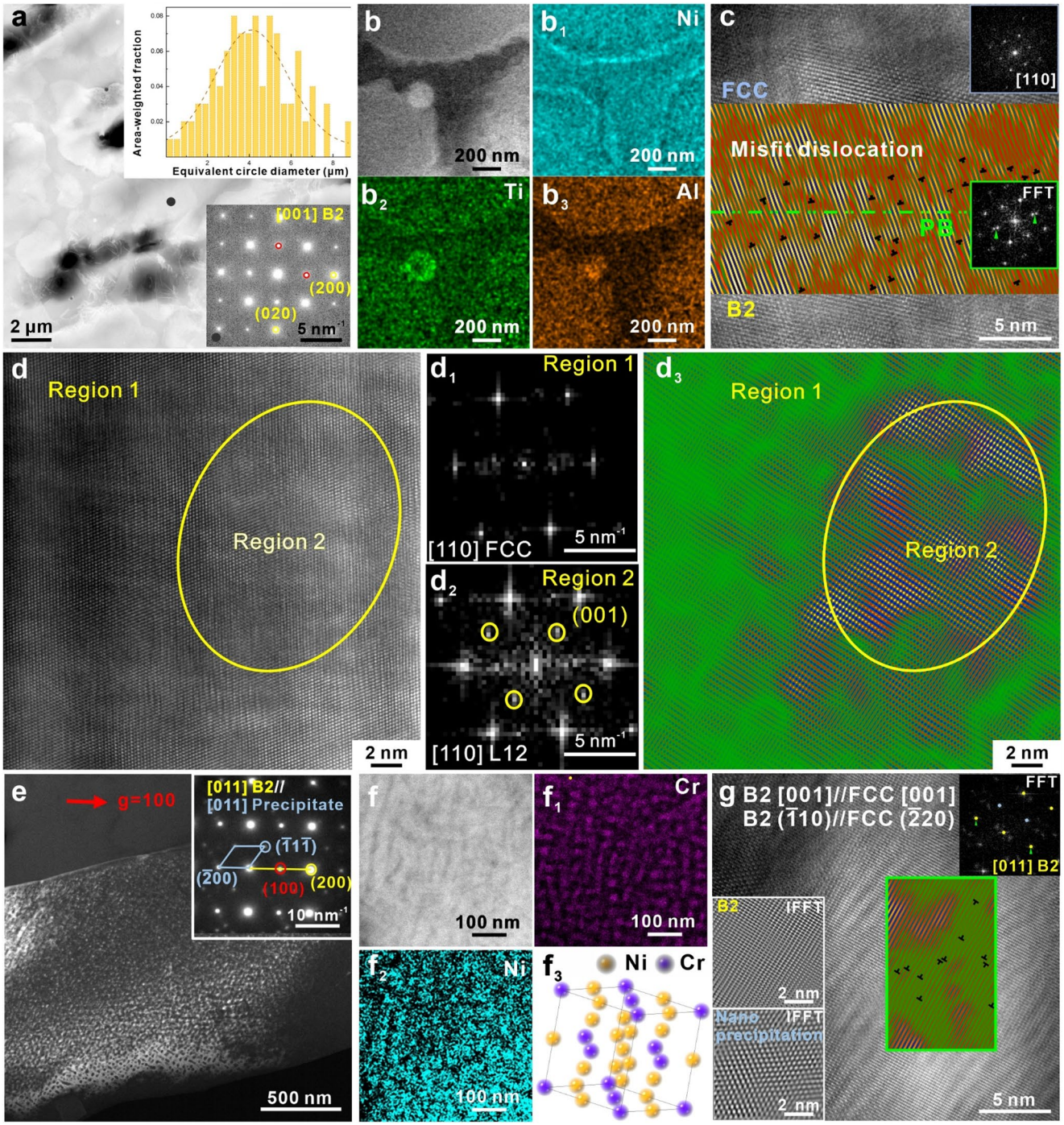

Fig. 4 Multi-scale structure and chemistry of the AM-EHEA-Ti samples. (**a**) The STEM image with grain size distribution and SADP inset confirming the B2 matrix. (**b**) The STEM-HAADF image with element mapping: (b_1) Ni segregating along the grain boundaries, (b_2) Ti segregating with (b_3) Al. (**c**) The HRTEM of the B2/FCC boundary (FFT inset) reveals misfit dislocations due to Ti-driven lattice distortion. (**d**) The HRTEM image and corresponding FFT patterns of (d_1) the FCC phase and (d_2) $L1_2$ phase with (d_3) IFFT image highlighting nanoscale ordered $L1_2$-type nanoparticles. (**e**) The dark-field image along *g*=[100], corresponding to the B2 [011] spot of the SADP inset, showing the precipitates inside the B2 phase. (**f**) The STEM-HAADF image with element mapping showing the (f_1) Cr and (f_2) Ni-rich precipitates, with (f_3) $D0_3$-FCC lattice structure. (**g**) The HRTEM micrograph showing the atomic-level B2 and nano-precipitates taken along [001] B2 zone axis with FFT inset, and the corresponding IFFT patterns of the B2 matrix and nano-precipitates

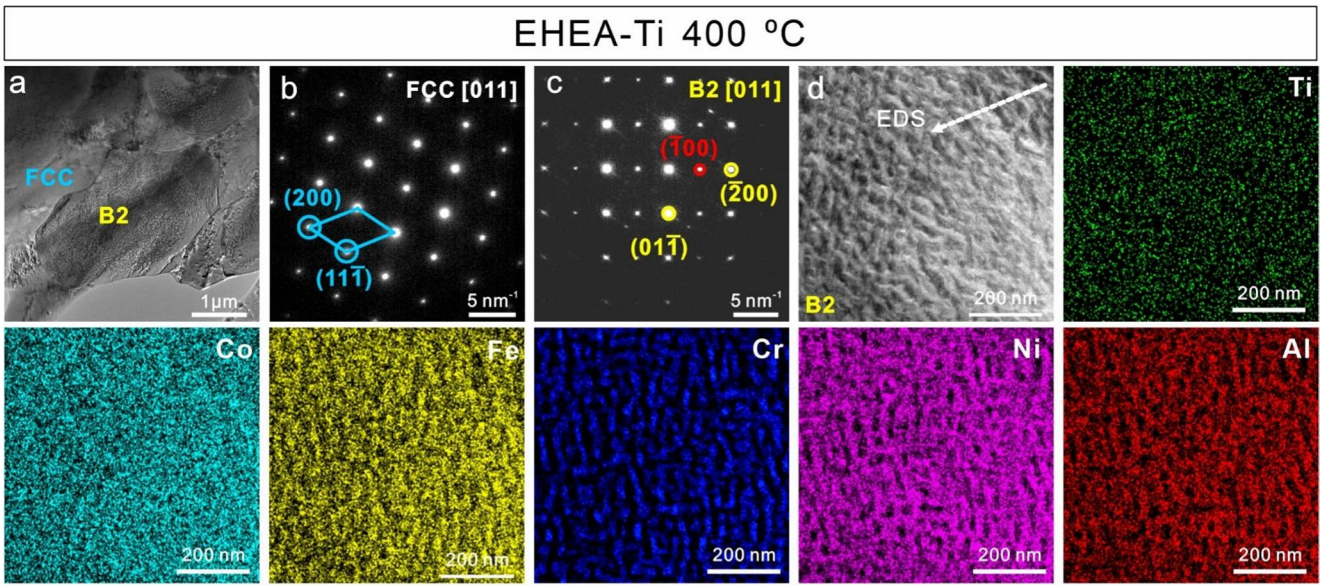

Fig. 5 Intermediate-temperature phase evolution in AM-EHEA-Ti before deformation at 400 °C: (**a**) The STEM-HAADF image with SADP, (**b**) along FCC [011] zone, and (**c**) B2 [011] zone indicating dissolution of $L1_2$ and $D0_3$.(**d**) The STEM-HAADF image with EDX line scanning in Fig. S6a and element mapping revealing homogeneous Ti/Co distribution, and striped-shaped Fe/Cr element clusters, Ni/Al element clusters in B2 phase, indicating spinodal decomposition

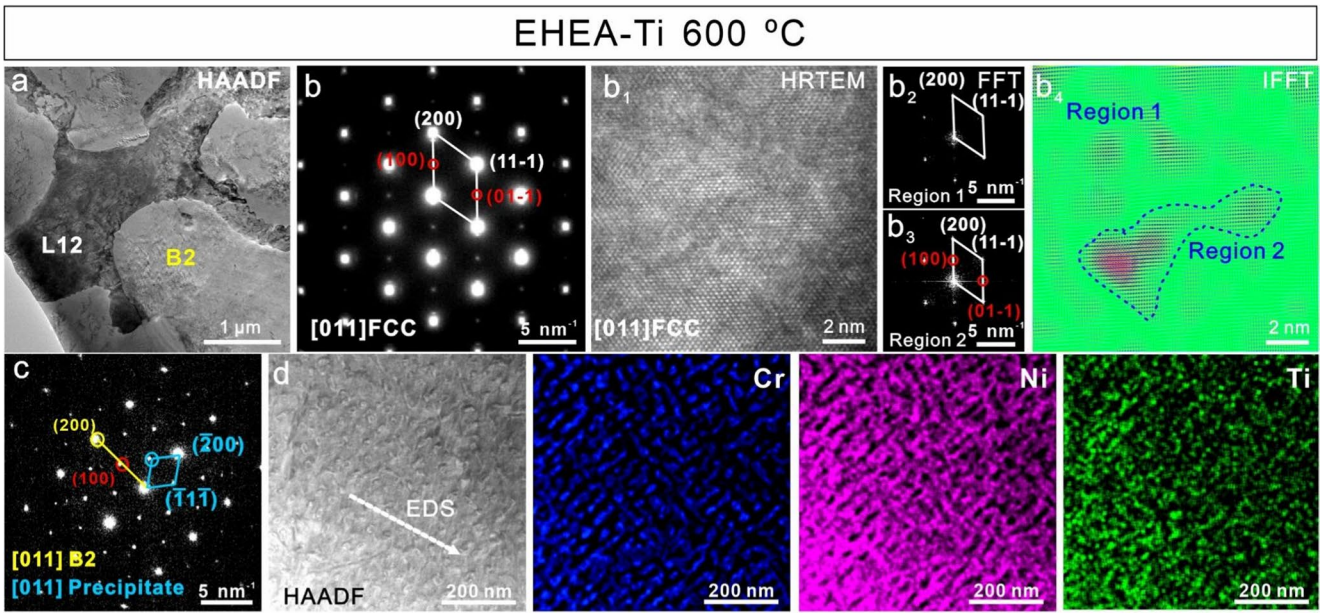

Fig. 6 Intermediate-temperature phase evolution in AM-EHEA-Ti before deformation at 600 °C: (**a**) STEM-HAADF image with SADP showing (**b**) FCC matrix along [011] zone with reprecipitated $L1_2$ phase. (b_1) The HRTEM image with corresponding FFT patterns of (b_2) the FCC phase, (b_3) $L1_2$ phase and (b_4) IFFT image of the $L1_2$-type nanoparticles. (**c**) The SADP of B2 along [011] zone axis confirming the reprecipitation of $D0_3$-FCC phase. (**d**) The STEM-HAADF image with EDX line scanning in Fig. S6b and element mapping revealing the matrix keeping striped-shaped Cr/Ni/Ti spinodal decomposition

positive mixing enthalpy between Cr and Ni (+ 4 kJ/mol) drives their mutual segregation: line scan analysis across the enlarged B2 region (Fig. 5d) reveals distinct Cr-rich and Ni-rich phase separation (Fig. S6a). EDX elemental mapping further demonstrates classic spinodal decomposition characteristics—while Ti and Co remain uniformly distributed, alternating Ni/Al-rich (ΔH_{mix} = − 22 kJ/mol) striped and Cr/Fe-rich striped regions emerge, reflecting their differential mixing enthalpies and relative diffusion mobilities. The positive mixing enthalpy of + 4 kJ/mol between Cr-Ni systems [37] creates an energy barrier that drives the segregation of Ni/Al-enriched regions from the remaining matrix.

Simultaneously, the larger atomic radii of Ti and Al [43] (1.47 Å and 1.43 Å, respectively) compared to Cr (1.25 Å) and Fe (1.26 Å) introduce significant lattice mismatch, generating additional strain energy that provides a strain relief pathway for spinodal decomposition [44]. Due to the slower diffusion kinetics of Ti and Co elements (Ti diffusivity in B2: $D \approx 10^{-21}$–10^{-20} m²/s) [45], this structure exhibits a ''diffusion lag'' effect, resulting in spinodal decomposition with extremely fine wavelengths (~ 10–20 nm) while effectively suppressing coarsening behavior. Consequently, the B2 matrix phase achieves compositional modulation through systematic elemental redistribution.

When the temperature is raised to 600 °C, HAADF imaging in Fig. 6a reveals that the equiaxed grain structure retains its morphology and dimensional stability. Renewed atomic rearrangement triggers reprecipitation of the $L1_2$ phase, as a superlattice spot (100) in Fig. 6b. The HRTEM imaging (Fig. 6b_1) with corresponding FFT (Figs. 6b_2-b_3) and IFFT (Fig. 6b_4) analyses confirm that these secondary $L1_2$ particles are exceptionally fine (< 10 nm), significantly smaller than those in the as-built state. The SADP along B2 [110] (Fig. 6c) further verifies the reformation of $D0_3$ precipitates. Finally, HAADF-STEM (Fig. 6d) coupled with a local line scan (Fig. S6b) demonstrates Cr/Ni re-clustering at a near 3:1 stoichiometry, indicating that Ti's connecting with Ni (−10 kJ/mol) modification of the local electronic environment promotes $D0_3$ nucleation [5] on the spinodal decomposed Cr/Ni(Ti)-enriched substrate (Fig. 6d). Together, these observations reveal a temperature-dependent interplay of dissolution, spinodal decomposition, and reprecipitation in AM-EHEA-Ti, driven by Ti-induced lattice distortion and element-specific thermodynamics.

4 Discussion

4.1 Additive manufacturing triggered an enhanced hardness in multicomponent Ti-containing EHEAs

The grain size distribution, phase maps, and grain boundary analysis obtained by EBSD in Fig. 7 demonstrate the exceptional microstructural stability achieved in AM-EHEA-Ti. At room temperature, both alloys exhibit similar initial grain size distributions with AM-EHEA showing 60% of grains in the 2–5 μm range (average 3.8 ± 1.3 μm) and AM-EHEA-Ti displaying 76.8% of grains in the same size range (average 3.3 ± 1.7 μm) as shown in Fig. 7a and d. However, pronounced differences emerge at intermediate temperatures where AM-EHEA undergoes significant microstructural instability, with 88.6% of grains coarsening to 5–10 μm at 400 °C (average 5.1 ± 1.3 μm, Fig. 7b) and maintaining 87.2% in the 5–10 μm range at 600 °C (average 6.3 ± 3.2 μm, Fig. 7c), indicating substantial grain growth and size redistribution. In contrast, AM-EHEA-Ti exhibits remarkable thermal stability, retaining 79.8% of grains in the refined 2–5 μm range at 400 °C (average 4.0 ± 1.4 μm, Fig. 7e) and maintaining 84.7% of grains below 5 μm at 600 °C (average 5.3 ± 0.9 μm, Fig. 7f), demonstrating exceptional resistance to thermally induced grain coarsening across the entire temperature range. Even more critically, the B2 phase content analysis reveals dramatic instability in AM-EHEA with phase fractions exhibiting complex, non-monotonic behavior that initially decreases from 23% at room temperature to 18% at 400 °C, followed by a dramatic increase to 50% at 600 °C, indicating severe temperature-sensitive phase transformations with unpredictable structural evolution that compromises material reliability in Fig. 7g. Conversely, AM-EHEA-Ti maintains exceptional phase stability with B2 content changing minimally from 93% at room temperature to 82% at 400 °C and 80% at 600 °C, representing only a 13% total variation compared to the 27% fluctuation range in the Ti-free alloy. The grain size evolution via Ti addition and temperature increase is summarized in Fig. 7h. Both AM-EHEA and AM-EHEA-Ti exhibit temperature-induced grain coarsening, yet their thermal stability differs markedly. AM-EHEA shows significant grain growth and structural instability at elevated temperatures, whereas AM-EHEA-Ti effectively suppresses coarsening, maintaining a refined grain structure across the entire temperature range.

In AM-EHEA-Ti, Ni element enrichment at grain boundaries significantly impedes grain boundary migration. These solute drag and Zener pinning mechanisms effectively suppress grain growth [46]. Additionally, Ti addition promotes the formation of Cr-rich $D0_3$ precipitates and B2 phases, which remain stable at 600 °C, thereby enhancing grain thermal stability [47]. These nanoscale thermally stable precipitates dispersed throughout the matrix provide strong pinning effects on dislocations and grain boundaries, enabling AM-EHEA-Ti to maintain fine grains (predominantly < 5 μm) and nearly constant B2 phase content across the 400–600 °C temperature range [46]. The stabilization mechanism of Ti addition against the B2 to FCC phase transformation can be calculated via classical nucleation theory the change in free energy for a new phase nucleus [48]: $\Delta G = -\frac{4\pi}{3} r^{*3} (\Delta G_V + \Delta G_E) + 4\pi r^{*2} \gamma$, ΔG is The system free energy change, r^* is the newly formed FCC phase nucleates treated as spherical precipitates with critical radius, ΔG_V is the negative chemical driving force, ΔG_E is the positive volumetric strain energy, γ is interfacial energy. In addition, with its significantly larger atomic radius (~ 1.47 Å) compared to other matrix elements (Ni ~ 1.25 Å, Al ~ 1.43 Å), it introduces substantial lattice distortions when FCC precipitates change from the B2 matrix. This atomic size mismatch ($\Delta r/r \approx 15.6\%$

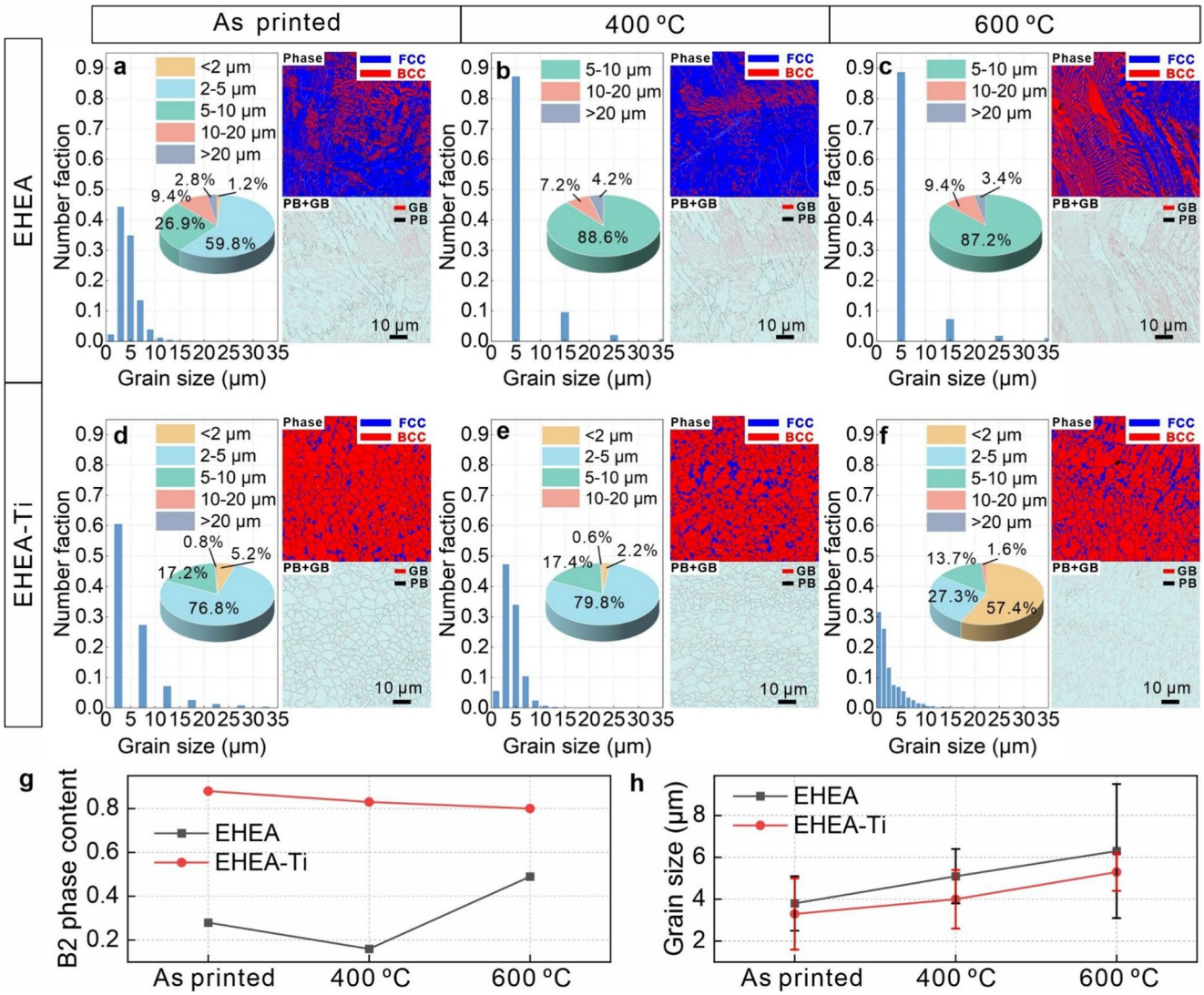

Fig. 7 Temperature-dependent EBSD analysis of AM-EHEA and AM-EHEA-Ti. Grain size distribution and phase map for AM-EHEA at: (**a**) room temperature, (**b**) 400 °C, (**c**) 600 °C. Grain size distribution and phase map for AM-EHEA-Ti: (**d**) room temperature, (**e**) 400 °C, (**f**) 600 °C. (**g**) B2 phase fraction variation changing with temperature for AM-EHEA-Ti*x* samples. (**h**) Average grain size variation changing with temperature for both alloys

for Ti-Ni pairs) dramatically increases the volumetric strain energy following $\triangle G_E = E \cdot (\triangle r/r)^2$, where E is the elasticity modulus, as a constant, which in turn elevates both the critical nucleus radius r^* and the nucleation barrier ΔG^* required for phase transformation. To achieve the same net driving force $|\triangle G_v + \triangle G_E|$, the system must overcome increasingly higher energy barriers, thereby kinetically retarding the B2 to FCC transformation. Simultaneously, Ti provides chemical stabilization through highly negative Ti-Ni and Ti-Al mixing enthalpies, which promote more exothermic B2 formation and lower the free energy of the ordered B2 phase, consequently reducing the chemical driving force for transformation to disordered FCC. These dual effects—enhanced elastic mismatch energy and strengthened chemical stability—work synergistically with the inherently sluggish diffusion characteristic of HEAs to create vastly enlarged nucleation barriers [49]. The result is effective kinetic trapping of the B2 phase even at intermediate temperatures, where the nucleation barrier curve (ΔG^* vs. r^*) for Ti-containing alloys peaks at significantly higher values than Ti-free compositions, thus strongly suppressing unwanted B2 to FCC phase transformation and maintaining the desired ordered microstructure across broader processing windows.

AM-EHEA-Ti stabilizes the B2 phase structure through strong intermetallic bonding and creates thermal barriers against grain boundary migration via precipitation pinning effects and solute drag mechanisms. This observation aligns with the empirical correlation that strength (ΔUTS = 1017 − 713 = 304 MPa at 600 °C, as shown in Fig. S1) is

approximately three times the hardness [50]. This combination enables AM-EHEA-Ti to maintain reliable mechanical performance under intermediate-temperature service, providing advantages over conventional or Ti-free materials.

4.2 Self-hardening ability via friction-induced phase evaluation at 600 °C

Based on the previously observed differences in COF and wear rate at 600 °C, the worn microstructure after sliding at this temperature was chosen for detailed subsurface analysis. The cross-sectional microstructure beneath the sliding surface along the sliding direction after deformation at 600 °C is examined to identify crack initiation sites and investigate subsurface structural changes of AM-EHEA during wear (Figs. 8a-a_1). Micro-scale cracks are clearly observed in Figs. 8a_2-a_3, revealing the microscopic damage mechanisms operating within the subsurface region. Figure 8b presents an HAADF-STEM image showing the FIB-prepared sample beneath the wear track, covering approximately 10 μm × 10 μm. The microcracks propagate during repeated sliding cycles, ultimately forming wear debris through the progressive detachment of material. The enlarged view of the substructure beneath the debris clearly reveals the loss of the original lamellar structure with grain fracture, evidenced by the corresponding SADP pattern in Fig. 8c. Furthermore, the rotation of the substructure zone demonstrates the formation of refined lamellar layers with a thickness reduced to less than 100 nm (Fig. 8d), with the corresponding SADP patterns in Figs. 8d_1-d_2 confirming the deterioration of the K-S orientation relationship along the FCC [011] direction. This microstructural degradation represents a critical transition from the initial coherent lamellar arrangement to a disordered, fractured state that significantly compromises the material's load-bearing capacity and accelerates wear progression.

Figure 9a shows the FIB-sectioned AM-EHEA-Ti sample tested at 600 °C, targeting the subsurface region beneath the wear track to investigate Ti's crucial role in microstructural stabilization under intermediate tribological conditions. Further, the HAADF-STEM image in Fig. 9b reveals the complex microstructural evolution. The corresponding SADP pattern in Fig. 9b_1 confirms the stable coexistence of $D0_3$ precipitates along with noticeable B2 matrix grain rotation caused by frictional shear, while Fig. 9b_2 presents the FCC SADP from the same region, confirming the stable presence of $L1_2$ phase throughout the wear deformation. The persistence of both precipitate phases suggests thermal stability at 600 °C and the ability to withstand substantial shear stress without dissolving or transforming, helping maintain strength. The observed grain rotation implies the material accommodates severe shear deformation by rotating existing grains rather than extensive grain boundary migration or recrystallization. Elemental mapping of the worn subsurface (Figs. 9b_3-b_4) provides further insight into the chemical partitioning and the role of Ti. Crucially, Ti remains segregated in the B2 phase even after wear at 600 °C, while Ni accumulates at grain boundaries, creating an elemental drag effect that effectively resists grain boundary migration during temperature elevation and contributes to microstructural stability. Ti acts as an anchor for the B2 phase, and Ni at grain boundaries acts as a barrier to grain movement, synergizing to stabilize the microstructure under thermal-mechanical stress [40, 51]. The bright-field (BF) TEM image

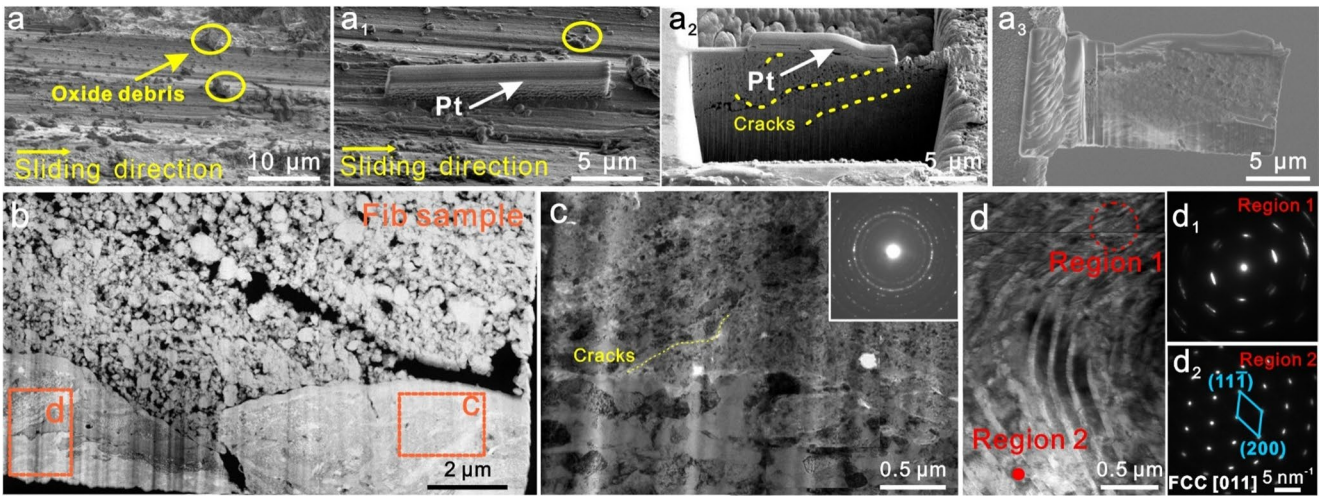

Fig. 8 Subsurface characterization of the AM-EHEA alloy after dry sliding at 600 °C. (**a**) SEM image of the wear track after sliding, (**a_1**) the selected representative location with the protective platinum (Pt) cap layer for subsurface analysis; (**a_2**) and (**a_3**) are low and high-magnification SEM images of the selected cross-sectional microstructure along the sliding direction, respectively. (**b**) HAADF-STEM image. (**c**) The enlarged HAADF-STEM image and corresponding SADP pattern of the deformed layer. (**d**) The enlarged HAADF-STEM image with the corresponding (d_1-d_2) SADP pattern along FCC [110] showing the grain rotation after deformation

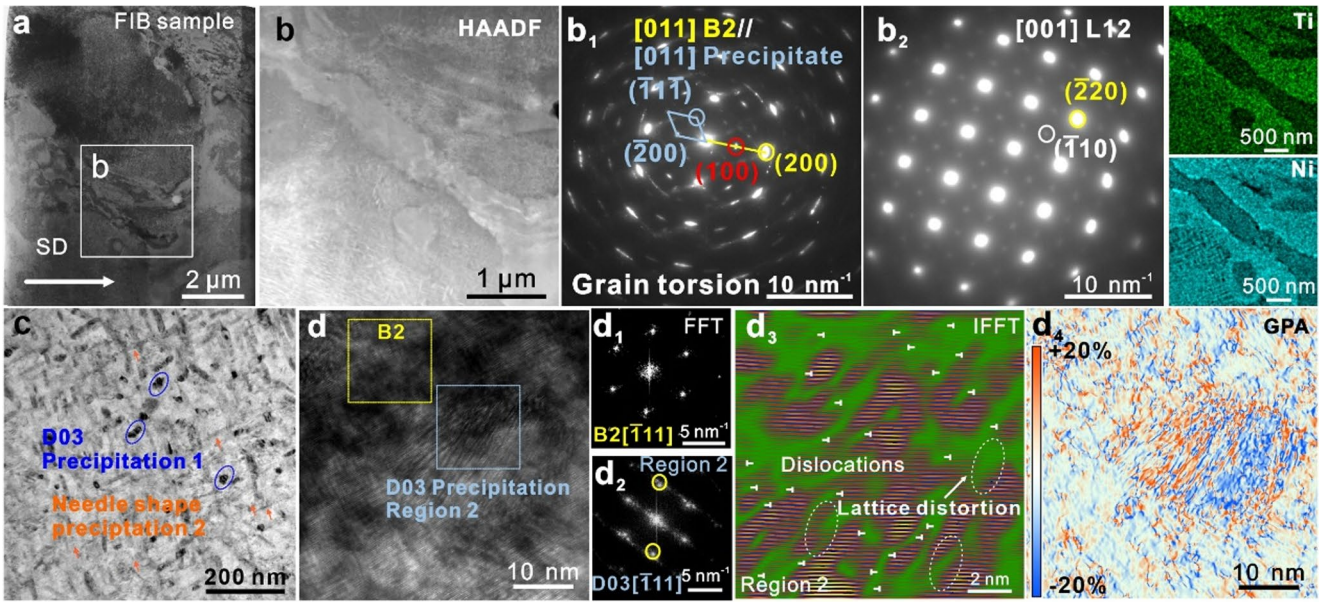

Fig. 9 Subsurface characterization of the AM-EHEA-Ti alloy after dry sliding at 600 °C. (**a**) HAADF-STEM image. (**b**) The enlarged HAADF-STEM image with corresponding SADP pattern (**b$_1$**) along the B2 [011] of the deformed layer showing the grain rotation and (**b$_2$**) showing the existence of the $L1_2$ phase along [001] axis, with the EDS mapping showing Ti/Ni elements distribution. (**c**) The enlarged BF-TEM image showing the $D0_3$ precipitation and the newly formed needle-shaped precipitation. (**d**) The HRTEM image and corresponding FFT patterns of (**d$_1$**) the B2 phase, (**d$_2$**) the $D0_3$ precipitation, and (**d$_3$**) the IFFT showing the lattice distortion, with (**d$_4$**) the GPA of the HRTEM in (**d**) showing the strain-bearing ability

in Fig. 9c reveals that beyond the $D0_3$ precipitates, newly formed needle-shaped precipitates have emerged within the B2 phase induced by the wear process. Under intense frictional shear and thermal exposure, the supersaturated B2 matrix becomes locally unstable, triggering nucleation of Ni-rich needle precipitates. The severe mechanical stress and frictional heating provide energy and atomic mobility necessary for Ni redistribution from the B2 solid solution into new phases during wear. The corresponding HRTEM analysis of $D0_3$ precipitates in Fig. 9d, with FFT and IFFT patterns (Figs. 9d_1-d_3), demonstrates a high dislocation density and considerable lattice distortion within precipitates, while geometric phase analysis (GPA) in Fig. 9d_4 illustrates the internal strains and enhanced strain-bearing ability of $D0_3$ precipitates within the B2 matrix, improving load transfer capacity during wear. Such distortion indicates that $D0_3$ particles absorb plastic deformation by accumulating dislocations while maintaining their ordered structure, acting as strong yet pliable reinforcements that trap dislocations to impede their motion, thereby accommodating deformation without fracturing to enable effective load sharing.

Figure 10a presents an enlarged HAADF-STEM image of the needle-shaped precipitates with line scanning analysis in Fig. 10a_1, revealing that these needle-shaped precipitates are primarily composed of Ni elements while the matrix retains its striped-spinodal-decomposed structure, which contribute the supersaturated Ni elements partition in unique AM structure (Figs. 10a_1), with the key distinction being that the friction process promotes Ti-Ni (−10 kJ/mol) interaction under applied stress, where Ni vacancy formation during precipitation development provides accommodation sites for Ti atoms. Since these precipitates were absent before deformation, the alloy exhibits an adaptive self-hardening response by dynamically forming strengthening phases under 600 °C tribological conditions. These needle-like precipitates, characterized by lengths of 210 ± 36 nm and widths of 18 ± 10 nm with intersecting angles of ~ 101.6°, create a network that subdivides the B2 grains into multiple cellular structures. This cellular subdivision effectively distributes applied stresses across multiple interfaces, mitigating stress concentration and enhancing the material's wear resistance through improved load-bearing capacity and mitigating the stress concentration mechanisms [52].

The HRTEM analysis along B2 [$\bar{1}$11] direction in Fig. 10b, with enlarged views in Fig. 10b_1 showing the B2 matrix and Fig. 10b_2 revealing the needle-shaped precipitation, confirms that these precipitates adopt an HCP structure, which formed in situ via a shear-induced transformation of the B2 phase during the wear process [53]. The atomic arrangement confirms the phase transformation from BCC to HCP with specific orientation relationships: BCC ($\bar{1}$12)// HCP (11 $\bar{2}$0) and BCC (110)//HCP ($\bar{1}$100). This correspondence is characteristic of martensitic-like transformation, where coordinated lattice shear produces a new phase with minimal long-range diffusion. The intense torsional stresses

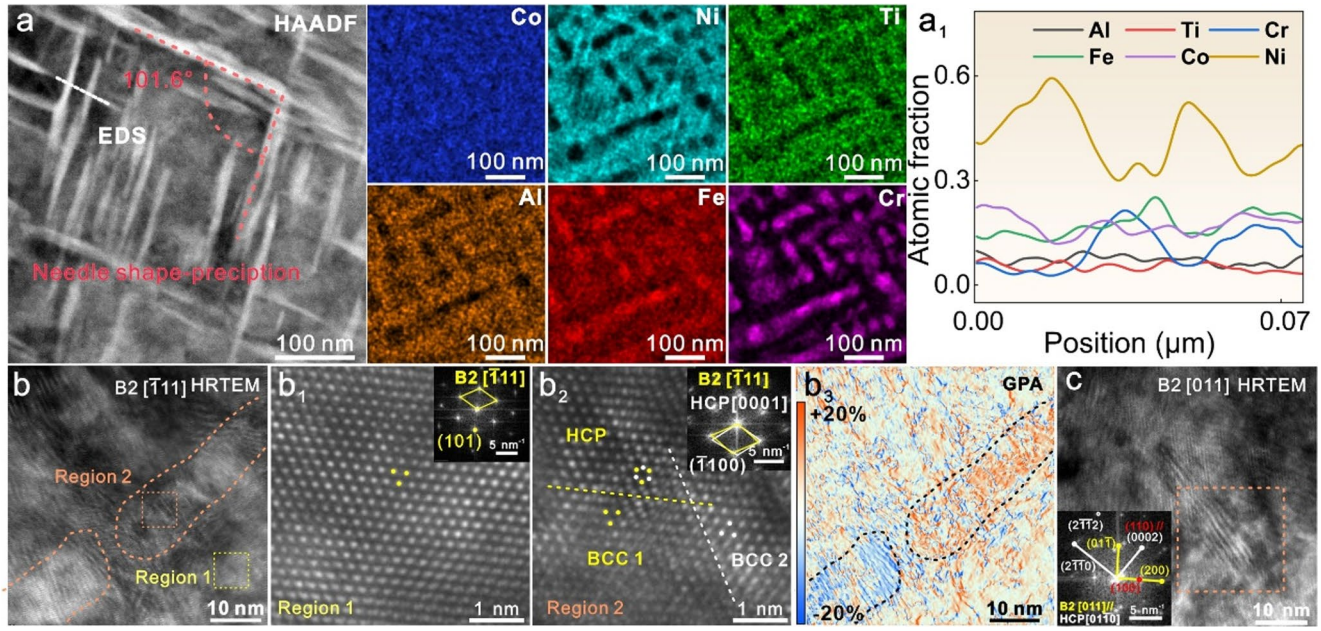

Fig. 10 Wear-induced needle-shaped precipitation characterization. (**a**) The enlarged HAADF-STEM image with the mapping showing the elements distribution with spinodal decomposition matrix, and the EDX (**a**$_1$) line scanning showing the precipitation with Ni-rich. (**b**) The HRTEM image and the enlarged HRTEM along B2 [$\bar{1}$ 11] showing (**b**$_1$) B2 matrix, and (**b**$_2$) HCP needle-shaped precipitation, with (**b**$_3$) the GPA of the HRTEM in (**b**) showing the strain-bearing ability. (**c**) The HRTEM image along B2 [011] and the HCP [01 $\bar{1}$0]

from friction drive segments of the B2 matrix, particularly Ni-enriched zones, to rearrange into HCP stacking, creating a finely dispersed HCP phase dynamically embedded throughout the B2 matrix during deformation. The stress-induced transformation exemplifies the alloy's adaptive microstructural evolution under load, where portions of the original BCC matrix shift directly into HCP structure in response to applied shear stress [54]. GPA (Fig. 10b$_3$) reveals significant localized strain surrounding needle precipitates, demonstrating the exceptional strain-bearing capability of this wear-induced transformation. The HCP phase formation within the B2 matrix endows the alloy with pronounced self-hardening characteristics, where microstructural evolution actively generates new phases and strain fields that elevate deformation resistance, fundamentally differing from typical intermediate-temperature wear responses of softening or coarsening. The lattice distortions and new phase interfaces create fresh dislocation obstacles, while the wear procedure generates additional impediments to further deformation, establishing a self-hardening, adaptive tribological response. Additional HRTEM imaging along the B2 [011] direction (Fig. 10c) reveals needle-shaped precipitates arranged in an alternating pattern, with adjacent needles oriented nearly perpendicular to each other. This interlocking network of reinforcing domains crisscrosses the original B2 grains, greatly enhancing strain accommodation and resistance. Under sliding wear, local contact stresses at microscopic surface peaks drive dislocation glide, leading to subsurface plastic deformation and material removal. The multi-directional precipitate arrangement ensures dislocations encounter precipitate/matrix interfaces regardless of glide direction, with each precipitate acting as a strengthening barrier that blocks or deflects dislocation motion. This dynamic microstructural evolution—achieved during service via the shear transformation mechanism—is a key factor in the alloy's improved wear resistance [53], where the act of wear actively refines and strengthens the microstructure in real-time. The dynamic formation of HCP nano-precipitates under tribological loading represents a distinct "self-hardening" mechanism, fundamentally different from classical deformation processes. Unlike conventional work hardening, which stems from dislocation accumulation, this mechanism relies on a stress-induced phase transformation that creates new strengthening interfaces. It also differs from thermally-assisted dynamic precipitation, as the HCP phase is absent after static heating and is uniquely nucleated by frictional shear stress. Furthermore, in contrast to dynamic recrystallization—a high-temperature softening mechanism—this transformation counteracts thermal softening by generating a stable, fine-scale network of hard precipitates that impede dislocation glide and grain boundary sliding. This adaptive response, where the wear process itself catalyzes a strengthening microstructural evolution, is key to the alloy's sustained wear resistance at elevated temperatures.

The present findings demonstrate that Ti addition fundamentally transforms AM-EHEA into a self-hardening

system during tribological loading. Ti stabilizes existing precipitates while enabling the formation of Ni-rich HCP needles through shear-driven transformation, creating multi-directional dislocation barriers with exceptional strain-bearing capacity. Rather than degrading under elevated conditions, the alloy adapts and strengthens through in-situ microstructural evolution, establishing a promising pathway for engineering self-adaptive materials in severe tribological applications.

4.3 Enhanced oxidation resistance in multicomponent Ti-containing EHEAs

Figure 11 systematically demonstrates the profound effect of Ti addition on oxidation behavior in AM-EHEA-Ti at intermediate temperatures. The AM-EHEA exhibits severe oxidative damage at 400 °C (Fig. 11a) with oxygen content reaching 22.98% (Fig. 11a_1), where SEM observations reveal extensive oxidation patches with oxide debris accumulation and surface tearing (Fig. 11b). Cross-sectional analysis shows lamellar structure refinement accompanied by multiple oxide formations, including Al- (Fig. 11c), Cr-, Fe-, Co-, and Ni-type oxides (Figs. 11c_1-c_5), indicating unselective non-protective oxidation processes. Damage worsens at 600 °C (Fig. 11d), with oxygen rising to 33.42% (Fig. 11d_1), and the enlarged SEM image in Fig. 11e clearly demonstrates an extensive thick oxide layer tearing, indicating a destructive cycle of repeated oxide deposition, fracture, and re-oxidation. The cross-sectional interface analysis in Figs. 11f-f_1 under the wear track reveals catastrophic oxidation damage where the subsurface lamellar structure is completely fractured and loses its original morphology, thick and fragmented oxide layers are crushed, and oxide cracks extend deep into the subsurface structure, resulting in complete loss of load-bearing and load-transferring capabilities. Enlarged HAADF-STEM with corresponding elemental mapping in Figs. 11f_2-f_8 confirms a pervasive oxidation layer over 3.1 μm involving all constituents, indicating a comprehensive oxidative reaction during wear. In Fig. 11f_2, clearly see the cracks in the oxidation layer cycle broken and stacked as the oxide debris.

In contrast, AM-EHEA-Ti demonstrates remarkable oxidation resistance across both temperature regimes, where at 400 °C (Fig. 11g) the wear track exhibits predominantly plastic flow with minimal oxide debris and oxygen content reduced to 15.19% (Fig. 11g_1) representing a 34% reduction compared to the Ti-free alloy, while crucially maintaining intact equiaxed grain structure in the subsurface (Fig. 11h) that preserves mechanical integrity. The SEM-EDX elemental mapping results are presented in Figs. 11i-i_5 clearly demonstrates that Al/Co/Cr/Fe serves as the primary element undergoing oxidation during the wear process of AM-EHEA-Ti under the tested conditions. Notably, the analysis reveals no significant participation of Ti in the oxidation reactions. At 600 °C, the addition of Ti significantly enhances the protective performance, as evident in the SEM images (Fig. 11j) and their enlarged view (Fig. 11k). Notably, no oxide debris or severe tearing is observed, and only plastic flow features are present. The oxygen content plunges to 10.17% (Fig. 11j_1), representing a 70% reduction relative to the Ti-free material. The subsurface cross-sectional oxidation layer analysis via HAADF-STEM (Fig. 11l) with corresponding element distribution reveals pronounced Al enrichment dense oxide film near the surface, with detailed composition mapping (Figs. 11l_1-l_7) confirming that oxidation is dominated exclusively by Al_2O_3 and Cr_2O_3 formation. Raman spectroscopy results in Fig. 11m provide critical mechanistic insights, showing that AM-EHEA at 400 °C contains multiple oxide phases including Cr_2O_3, Al_2O_3, Co_3O_4, NiO, and Fe_3O_4 [55–60], while at 600 °C, Fe_2O_3 formation is also observed, indicating progressive oxidation of multiple elements. In contrast, AM-EHEA-Ti at 400 °C exhibits a significantly simplified oxide chemistry, with only Al_2O_3, Cr_2O_3, NiO, and Fe_3O_4 detected. Most strikingly, at 600 °C, only Al_2O_3/Cr_2O_3 remains, demonstrating complete selective oxidation toward the most thermodynamically stable oxide. Meanwhile, EELS analysis of the cross-sectional oxidation layers confirms the elemental differences in oxidation behavior. In Fig. 11m_1 (AM-EHEA), the oxide layer contains all alloying elements, whereas Fig. 11m_2 demonstrates that only Al and Cr participate in oxidation, with oxide compositions shown in Table 3. The layered structure shows Al-O in direct contact with the sample surface, topped by a Cr_2O_3 outer layer, with partially discontinuous Fe/Ni/Co oxides in the intermediate region in Figs. 11l_1-l_7. Ti addition promotes selective oxidation of Al and Cr oxides. The oxide layer thickness measured by STEM-EDX is only 70.5 ± 4.1 nm, representing a 97.7% reduction in oxidation layer thickness, indicating that the Al and Cr oxide layers provide complete surface protection and further suppress oxidation behavior.

The oxidation suppression mechanism works through both thermodynamic and kinetic pathways. Thermodynamically, the Gibbs free energy ordering is CoO > Al_2O_3 > Cr_2O_3 > NiO > Fe_3O_4 [25], which favors Al_2O_3/Cr_2O_3 formation. But the mechanical properties matter more for tribological applications. Al_2O_3 and Cr_2O_3 have Vickers hardness values of 1500 HV and 1250 HV, respectively, significantly higher than CoO (610 HV), Fe_3O_4 (620 HV), and NiO (500 HV) [25]. This hardness difference is crucial-according to Archard's law [61], harder oxides resist destruction (Figs. 9 L-l_7) during sliding contact while softer ones get removed and turn into abrasive debris, while softer oxides are quickly removed, creating debris that acts as abrasive particles, as shown in Figs. 9f_2-f_8.

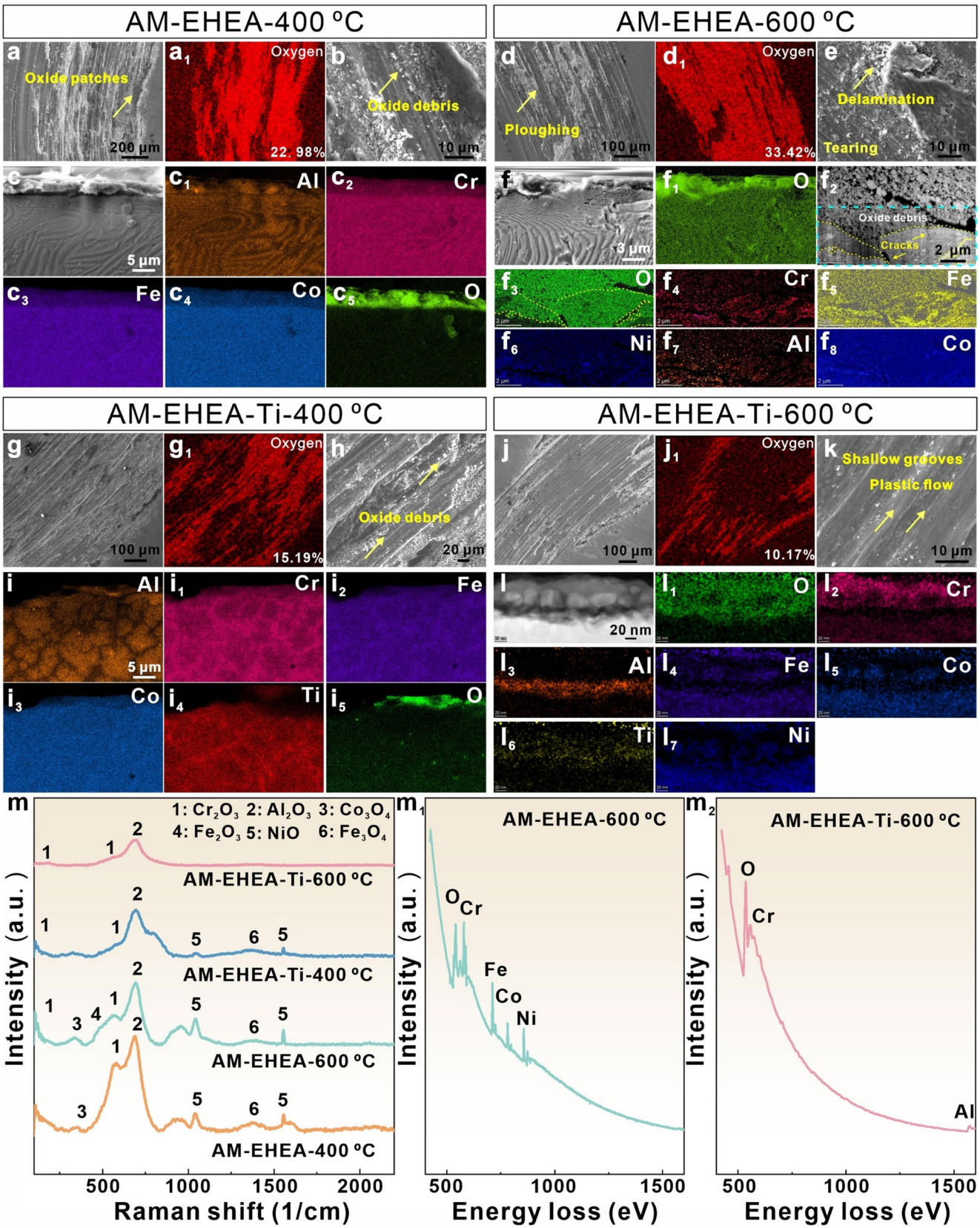
AM-EHEA-400 °C
AM-EHEA-600 °C
AM-EHEA-Ti-400 °C
AM-EHEA-Ti-600 °C
Oxide patches
Oxygen
Oxide debris
Ploughing
Delamination
Tearing
Oxide debris
Cracks
Shallow grooves
Plastic flow
1: Cr2O3 2: Al2O3 3: Co3O4
4: Fe2O3 5: NiO 6: Fe3O4
AM-EHEA-Ti-600 °C
AM-EHEA-Ti-400 °C
AM-EHEA-600 °C
Intensity (a.u.)
Raman shift (1/cm)
Energy loss (eV)

Fig. 11 SEM images of the worn surface morphologies directed to the contacting area at the sample surface after deformation. AM-EHEA at 400 °C: (**a**) top view with ($\mathbf{a_1}$) oxygen distribution and (**b**) enlarged top view. (**c**) Cross-section of subsurface with elements distribution: ($\mathbf{c_1}$) Al, ($\mathbf{c_2}$) Cr, ($\mathbf{c_3}$) Fe, ($\mathbf{c_4}$) Co, ($\mathbf{c_5}$) Oxygen. AM-EHEA at 600 °C: (**d**) top view with ($\mathbf{d_1}$) oxygen distribution and (**e**) enlarged top view. (f) Cross-section of subsurface with elements distribution: ($\mathbf{f_1}$) Oxygen, ($\mathbf{f_2}$) enlarged oxidation layer by HAADF-STEM, with corresponding element distribution: ($\mathbf{f_3}$) Oxygen, ($\mathbf{f_4}$) Cr, ($\mathbf{f_5}$) Fe, ($\mathbf{f_6}$) Ni, ($\mathbf{f_7}$) Al, ($\mathbf{f_8}$) Co. AM-EHEA-Ti at 400 °C: (**g**) top view with ($\mathbf{g_1}$) oxygen distribution and (**h**) enlarged top view. Cross-section of subsurface with elements distribution: (i) Al, ($\mathbf{i_1}$) Cr, ($\mathbf{i_2}$) Fe, ($\mathbf{i_3}$) Co, ($\mathbf{i_4}$) Ti, ($\mathbf{i_5}$) Oxygen. AM-EHEA-Ti at 600 °C: (**j**) top view with ($\mathbf{j_1}$) oxygen distribution and (**k**) enlarged top view. (**l**) Enlarged oxidation layer by HAADF-STEM, with corresponding element distribution: ($\mathbf{l_1}$) Oxygen, ($\mathbf{l_2}$) Cr, ($\mathbf{l_3}$) Al, ($\mathbf{l_4}$) Fe, ($\mathbf{l_5}$) Co, ($\mathbf{l_6}$) Ti, ($\mathbf{l_7}$) Ni. (**m**) Raman spectrum analysis from the outside of the worn surfaces of all the samples. High-loss EELS spectra acquired from the cross-section oxidation layer in ($\mathbf{f_2}$) and (**l**), respectively: ($\mathbf{m_1}$) AM-EHEA ($\mathbf{m_2}$) AM-EHEA-Ti

Kinetically, Ti addition changes the oxidation behavior through several pathways [62, 63]. Ti substitutes for Al in the B2 phase, and the negative Ti-Ni enthalpy (−10 KJ/mol) promotes Ni-rich precipitation within the matrix [27]. This pulls Ni/Cr out of solid solution, preventing unstable NiO/CrNiO formation while freeing up Al for oxidation. At 600 °C, $D0_3$ precipitates and Ni-rich needle precipitates further stabilize the microstructure [64]. Ti also creates lattice distortion that slows down diffusion significantly. The diffusion coefficients drop to $D_{Cr} \approx 10^{-18}$ m²/s and $D_{Ni} \approx 10^{-17}$ m²/s at 600 °C [65, 66], creating a "sluggish diffusion" effect that reduces interface and grain boundary transport. The intermediate (Fe, Ni, Co)-oxide layer becomes starved of material and can't thicken properly. The Al-O layer acts as an internal seal. It forms early at the metal-oxide interface and blocks both inward oxygen flux and outward cation migration. Ti makes this "valve effect" stronger, cutting off supply to the intermediate layer and limiting outer layer growth [62, 67, 68]. For the outer Cr_2O_3 layer, Ti acts as a conductivity-reducing dopant [69]. Cr_2O_3 typically exhibits p-type transport dominated by electron holes [70], and continued oxide growth needs coupled metal ion and electron/hole transport. The Ti-Cr negative enthalpy (−7 kJ/mol) is second only to Ti-Ni [37], so Ti^{4+} incorporation into the Cr_2O_3 lattice reduces mobile hole concentration and suppresses Cr^{3+} migration related to Cr vacancies [26, 71]. This blocks oxygen ion conduction, making the outer layer grow slower and denser [63]. The overall effect is that Ti suppresses the formation of (Ni, Co, Fe)-oxide and reduces total film thickness [69, 72].

Instead of the destructive oxide formation-destruction cycle seen in Ti-free alloys, the Ti-modified system builds a stable Al_2O_3/Cr_2O_3 protective layer. This thin, dense bilayer has high hardness, low conductivity, and good adhesion. It cuts down on spalling-regeneration cycles. The superior properties of this protective layer prevent deep oxidation, preserve subsurface integrity, and alter intermediate-temperature oxidation behavior through combined thermodynamic and kinetic control that favors the selective dominance of Al_2O_3 and Cr_2O_3.

4.4 Expectational tribology mechanism in multicomponent Ti-containing EHEAs

Figure 12 illustrates the temperature-dependent wear mechanisms in AM-EHEA-Ti alloys. The wear track surface (Fig. 12a) and 3D profile (Fig. 12a_1) quantify surface damage extent. At 400 °C, the Ti-free alloy exhibits complex wear involving both abrasive and oxidative mechanisms (Fig. 12b). Cross-sectional analysis reveals refined eutectic lamellae (< 100 nm thickness) extending 2.45 μm beneath the surface (Fig. 12b_1). Oxidative wear creates a destructive cycle where brittle oxide scales repeatedly fracture and spall, resulting in continuous material loss [73]. Simultaneously, abrasive wear generates deep surface grooves through micro-cutting and micro-plowing actions [74]. At 600 °C, deterioration intensifies (Figs. 12c-c_1) with wear damage penetrating 6.3 μm into the subsurface and extensive eutectic cracking. The deteriorated K-S orientation relationship reduces load-bearing capabilities. Multiple destructive mechanisms operate: intensified oxidative wear through faster oxidation kinetics, abrasive wear causing severe surface damage, three-body wear [75] from trapped debris acting as grinding media, adhesive wear from oxide spallation creating material transfer and surface tearing, and fatigue wear [76] as the dominant failure mode where repeated thermal cycling initiates subsurface crack nucleation, leading to catastrophic delamination and spalling.

Ti addition effectively mitigates these mechanisms. At 400 °C (Fig. 12d), the surface morphology primarily exhibits benign plastic deformation through ploughing, with suppressed oxide formation and minimal material tearing. Deep grooves parallel to sliding, with obvious plastic deformation and delamination [77], indicate controlled two-body abrasive wear [73], causing material displacement rather than removal. Cross-sectional analysis (Fig. 12d_1) confirms the underlying microstructure retains well-defined equiaxed grains, demonstrating enhanced thermal stability. The wear mechanism shifts to purely abrasive wear, characterized by

Table 3 Oxidation layer composition (by EELS) of EHEA and EHEA-Ti alloys at 600 °C via AM, respectively

	Al (at%)	Co (at%)	Cr (at%)	Fe (at%)	Ni (at%)	Ti (at%)	O (at%)
EHEA	0.0±0.5	7.4±0.7	1.60±0.17	9.8±1.0	12.1±1.2	/	69.1±1.6
EHEA-Ti	38.14±1.2	0.0±1.4	1.4±1.1	0.96±0.11	0±1.3	0.6±0.078	58.9±1.7

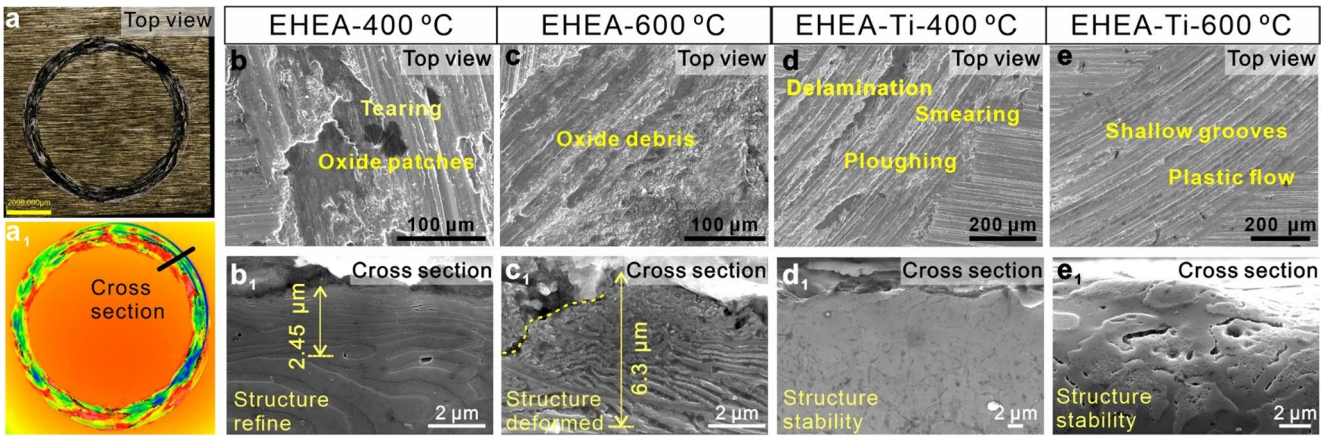

Fig. 12 Wear characteristics of the AM-EHEA-Ti*x* samples upon dry sliding at intermediate-temperature working conditions. (**a**) Optical image of wear track. (**a**$_1$) 3D surface profile of wear track. SEM images of the wear track: AM-EHEA at 400 °C: (**b**) top view, (**b**$_1$) cross section. AM-EHEA at 600 °C: (**c**) top view, (**c**$_1$) cross section. AM-EHEA-Ti at 400 °C: (**d**) top view, (**d**$_1$) cross section. AM-EHEA at 600 °C: (**e**) top view, (**e**$_1$) cross section

shallow grooves that result from material flow without significant removal, representing a fundamental transition from destructive to protective behavior. At 600 °C (Fig. 12e), the Ti-containing alloy exhibits a remarkable improvement, characterized by shallow sliding grooves and controlled plastic flow, indicating mild abrasive wear with reduced severity due to the formation of a protective surface layer acting as a lubricating barrier. Minor grain boundary cracks in the subsurface (Fig. 12e$_1$) critically do not propagate or evolve into severe damage, preventing the catastrophic fatigue wear observed in Ti-free alloys. The AM-fabricated equiaxed grain structure provides crack resistance through uniform stress distribution and multiple deflection paths [78], delaying damage accumulation and preventing sudden failure while maintaining dimensional stability. Critically, the wear grooves in Fig. 12e are shallower than those in Fig. 12d, despite the higher temperature, underscoring Ti's role in promoting stable, adherent protective oxide formation that transforms wear mechanisms from destructive material removal to protective surface modification. This layer acts as an effective barrier against direct metal contact, suppressing intermediate-temperature oxidation and preventing thermal softening, converting destructive oxidative wear into beneficial protection. Ti addition achieves remarkable transformation from the catastrophic combination of oxidative, abrasive, three-body, adhesive, and fatigue wear in Ti-free alloys to predominantly benign plastic deformation and mild abrasive wear, while promoting protective oxide formation with self-lubricating properties and stabilizing microstructure against thermal degradation, with AM-processed equiaxed grains contributing superior crack resistance through effective stress redistribution and deflection mechanisms. The significantly reduced and stabilized wear scar on the Si_3N_4 counterface, which slides against AM-EHEA-Ti (SI Fig. S5), provides direct evidence at the tribosystem level. This observation corroborates the proposed transition to a mild abrasive regime. The dense, adherent Al_2O_3/Cr_2O_3 scale on AM-EHEA-Ti not only protects the alloy surface but also minimizes abrasive ploughing and adhesive material transfer to the counterface. Consequently, the tribological interaction shifts from a destructive system (high wear on both surfaces) to a protective one, where the stable oxide layer acts as a barrier, significantly reducing wear on both the alloy and its counterpart.

Figure 13 provides a schematic comparison of wear mechanisms in AM-EHEA and AM-EHEA-Ti during 600 °C dry sliding. AM-EHEA, Fig. 13a, top view showing deep abrasive grooves and thick, fragmented oxide debris indicative of severe oxidative–abrasive wear. The cross-section reveals a thick oxide layer, severely degraded lamellar eutectic, and numerous subsurface cracks from the oxidation layer to the subsurface, leading to fatigue wear. The wear mechanisms shown in Fig. 13b are dramatically different. The top view of AM-EHEA-Ti reveals shallow grooves covered by a thin, uniform protective Al_2O_3/Cr_2O_3 layer, characteristic of mild abrasive wear. The cross-section illustrates the retained equiaxed grains (~4 μm), with the $D0_3$ and needle-shaped precipitations in the B2 phase. Only minimal surface deformation without crack propagation, indicative of stable intermediate-temperature wear performance. This marked improvement arises because AM processing generates ultrafine, homogeneous equiaxed structures and a high fraction of HAGBs with element distribution that distributes contact stresses uniformly and hinders crack initiation. The synergy of AM-induced ultrafine grain structures and Ti-driven phase stabilization transforms the wear mode from severe oxidative–abrasive fatigue in AM-EHEA to predominantly mild abrasive and plastic deformation in AM-EHEA-Ti, tailoring the alloy's microstructural characteristics and

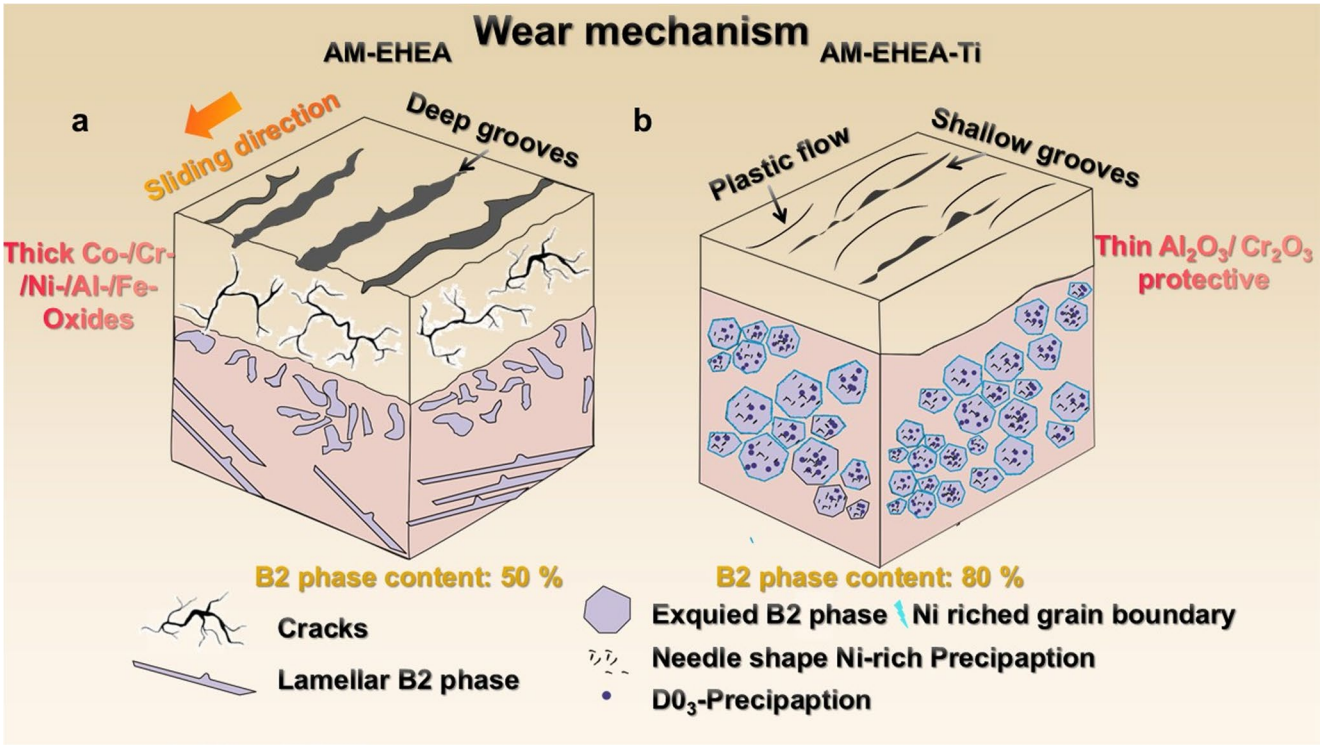

Fig. 13 Wear mechanism schematic at 600 °C. (a) AM-EHEA, (b) AM-EHEA-Ti

tribological behavior through enhanced phase stability and improved interfacial properties. Looking beyond the tested regime, the Ti-induced mechanisms of B2 stabilization and protective scale formation are anticipated to remain effective at temperatures exceeding 600 °C, potentially further enhancing oxidation resistance and microstructural stability under more extreme service conditions.

5 Conclusions

This study employs an AM-driven Ti-maintaining microstructural design, combined with phase stabilization, to develop a self-hardening, wear-adaptive material for intermediate-temperature applications. The key findings are summarized as follows:

1. LENS-ed $AlCoCrFeNi_{2.1}$ combined with 4.68 at% Ti generates an ultrafine equiaxed B2-dominated microstructure (3.3 ± 0.8 μm), featuring nanoscale $L1_2$ precipitates in FCC domains and $D0_3$ precipitates in the B2 matrix. Ti addition elevates the B2 phase fraction from 30.6% to 86.8%, while establishing a dense network of high-angle grain boundaries (91.2% HAGBs) with Ni segregation. This unique architecture enables synergistic strengthening via grain boundary hardening, Hall–Petch refinement, and precipitation mechanisms.
2. Under dry sliding at 600 °C, AM-EHEA-Ti exhibits a specific wear rate of 6.2×10^{-5} $mm^3/N \cdot m$—one order of magnitude smaller than AM-EHEA (3.20×10^{-4} $mm^3/N \cdot m$). Elemental segregation at grain boundaries impedes boundary migration, preserving microstructural integrity and suppressing substructure degradation. Selective formation of a protective Al_2O_3/Cr_2O_3 scale prevents cyclic oxidation and subsurface fragmentation.
3. The wear mechanism transitions from severe oxidative-abrasive-fatigue in AM-EHEA, characterized by thick, fragmented oxides and deep subsurface cracks, to mild abrasive and plastic flow in AM-EHEA-Ti, dominated by a protective Al_2O_3/Cr_2O_3 layer, stable equiaxed grains, and dynamic self-hardening via friction-induced HCP nanoprecipitates (Ni-rich needles) within the B2 matrix during wear.

Collectively, AM-EHEA-Ti optimizes wear-resistant mechanisms—grain-boundary stabilization, precipitation hardening, and oxide-scale protection—thereby transcending the limitations of conventional casting and existing HEAs. The strategy combines AM-enabled grain refinement and solute trapping with targeted alloying to control oxidation and stabilize phases. Key elements include rapid solidification, which creates metastable, refined microstructures prone to in-situ adaptation; alloying additions favor the formation of protective scales and stable strengthening phases under

service conditions. Optimal compositions require system-specific tuning, but the framework provides a route for designing wear-resistant alloys for intermediate-temperature applications.

Supplementary Information The online version contains supplementary material available at https://doi.org/10.1007/s42114-026-01649-2.

Author contributions **Yixuan Sun: ** Writing-review & editing, Writing-original draft, Methodology, Data curation, Conceptualization; **Chunjin Wang: ** Investigation, Data curation, Project administration, Supervision; **Rui Gao: ** Validation, Investigation; **Chuanxi Ren: ** Methodology, Writing-review; **Changning Bai: ** Writing-review; **Dingding Xiang: ** Writing-review; **Chi Fai Cheung: ** Supervision, Project administration, Funding acquisition; **Zibin Chen: ** Supervision, Project administration.

Funding Open access funding provided by The Hong Kong Polytechnic University. The work described in this paper was mainly supported by the research studentship from the Research and Innovation Office of The Hong Kong Polytechnic University (Project codes: RJHP, 1-W308, BBX5, CD9E, and UARQ) and the Shenzhen-Hong Kong-Macau Technology Research Program (Project No: SGDX20220530110804030 and SGDX20230821092100002). The authors would also like to express their sincere thanks to the funding support from the State Key Laboratories in Hong Kong from the Innovation and Technology Commission (ITC) of the Government of the Hong Kong Special Administrative Region (HKSAR).

Data availability The data that support the findings of this study are available from the corresponding author upon reasonable request.

Declarations

Competing interests The authors declare no competing interests.

References

1. Holmberg K, Erdemir A (2017) Influence of tribology on global energy consumption, costs and emissions. Friction 5:263–284. https://doi.org/10.1007/s40544-017-0183-5
2. Zhang Z, Hershkovitz E, An Q, Liu L, Wang X, Deng Z, Baucom G, Wang W, Zhao J, Xin Z, Moore L, Yao Y, Islam MRU, Chen X, Cui B, Li L, Xin H, Li L, Kim H, Cai W (2024) Spinel oxide enables high-temperature self-lubrication in superalloys. Nat Commun 15:10039. https://doi.org/10.1038/s41467-024-54482-w
3. Ren J, Zhang Y, Zhao D, Chen Y, Guan S, Liu Y, Liu L, Peng S, Kong F, Poplawsky J, Gao G, Voisin T, An K, Wang Y, Xie K, Zhu T, Chen W (2022) Strong yet ductile nanolamellar high-entropy alloys by additive manufacturing. Nature 608:62–68. https://doi.org/10.1038/s41586-022-04914-8
4. Liu W, Li Y, Gao D, He Y, Vasseghian Y, Hojjati-Najafabadi A (2025) Microstructure and properties of polycrystalline diamond with AlCoCrFeNi2.1 eutectic high-entropy alloys as binder. Adv Compos Hybrid Mater 8:124. https://doi.org/10.1007/s42114-025-01214-3
5. Sun Y, Wang C, Ren C, Zhang D, Li K, Cheung CF, Chen Z (2025) Multiscale chemical ordering heterogeneity facilitates exceptional strength and ductility in additively manufactured ti-added AlCoCrFeNi2.1 high-entropy alloys at intermediate temperatures. Int J Plast 190:104373. https://doi.org/10.1016/j.ijplas.2025.104373
6. Jiang Wei, Zhou Jian, Cao Yang, Meng Ao, Liu Runchang, Li Jiansheng, Li Zhuming, Zhao Yu, Zhao Yonghao (2025) Tribo-induced microstructural evolutions and wear mechanisms of AlCoCrFeNi2.1 eutectic high-entropy alloy at elevated temperatures. Acta Mater 296:121272. https://doi.org/10.1016/j.actamat.2025.121272
7. Liu C, Li Z, Lu W, Bao Y, Xia W, Wu X, Zhao H, Gault B, Liu C, Herbig M, Fischer A, Dehm G, Wu G, Raabe D (2021) Reactive wear protection through strong and deformable oxide nanocomposite surfaces. Nat Commun 12:1–8. https://doi.org/10.1038/s41467-021-25778-y
8. Nie S, Zheng Z, Qiao Y, Duan Y, Cui J, Mekkey SD, Amin MA, Melhi S, Yang H, Zhou H, Zheng S (2024) Corrosion behavior of as-cast Al0.75CoCr1.25FeNi high entropy alloy in 0.5 mol/L sulfuric acid. Adv Compos Hybrid Mater 7:138. https://doi.org/10.1007/s42114-024-00951-1
9. Zhou YH, Zhang JY, Zhang J, Yao XY, Luan JH, Li Q, Liu SF, Xiao B, Ju J, Zhao SJ, Zhao YL, Sun ZY, Nan H, Yan M, Yang T (2024) A strong-yet-ductile high-entropy alloy in a broad temperature range from cryogenic to elevated temperatures. Acta Mater 268:119770. https://doi.org/10.1016/j.actamat.2024.119770
10. Zamani MR, Mirzadeh H, Malekan M, Cao SC, Yeh J-W (2022) Grain growth in high-entropy alloys (HEAs): a review. High Entropy Alloys Mater 1:25–59. https://doi.org/10.1007/s44210-022-00002-8
11. Tang Z, Senkov ON, Parish CM, Zhang C, Zhang F, Santodonato LJ, Wang G, Zhao G, Yang F, Liaw PK (2015) Tensile ductility of an alcocrfeni multi-phase high-entropy alloy through hot isostatic pressing (HIP) and homogenization. Mater Sci Eng A 647:229–240. https://doi.org/10.1016/j.msea.2015.08.078
12. Tokarewicz M, Grądzka-Dahlke M (2021) Review of recent research on alcocrfeni high-entropy alloy. Metals 11:1302. https://doi.org/10.3390/met11081302
13. Lozinko A, Mishin OV, Yu T, Klement U, Guo S, Zhang Y (2019) Quantification of microstructure in a eutectic high entropy alloy AlCoCrFeNi2.1, IOP Conf. Ser : Mater Sci Eng 580:12039. https://doi.org/10.1088/1757-899X/580/1/012039
14. Chookajorn T, Murdoch HA, Schuh CA (2012) Design of stable nanocrystalline alloys. Science. https://doi.org/10.1126/science.1224737
15. Radhika N, Krishna SA, Basak AK, Adediran AA (2024) Microstructure and tribological behaviour of CoCrCuFeTi high entropy alloy reinforced SS304 through friction stir processing. Sci Rep 14:3662. https://doi.org/10.1038/s41598-024-54267-7
16. Wang J, Zhang B, Yu Y, Zhang Z, Zhu S, Lou X, Wang Z (2020) Study of high temperature friction and wear performance of (CoCrFeMnNi)85Ti15 high-entropy alloy coating prepared by plasma cladding. Surf Coat Technol 384:125337. https://doi.org/10.1016/j.surfcoat.2020.125337

17. Hamdi H, Abedi HR, Zhang Y (2023) A review study on thermal stability of high entropy alloys: normal/abnormal resistance of grain growth. J Alloys Compd 960:170826. https://doi.org/10.1016/j.jallcom.2023.170826
18. Faraji A, Farvizi M, Ebadzadeh T, Kim HS (2022) Microstructure, wear performance, and mechanical properties of spark plasma-sintered AlCoCrFeNi high-entropy alloy after heat treatment. Intermetallics 149:107656. https://doi.org/10.1016/j.intermet.2022.107656
19. Hariharan A, Lu L, Risse J, Kostka A, Gault B, Jägle EA, Raabe D (2019) Misorientation-dependent solute enrichment at interfaces and its contribution to defect formation mechanisms during laser additive manufacturing of superalloys. Phys Rev Mater 3:123602. https://doi.org/10.1103/PhysRevMaterials.3.123602
20. Ren N, Li J, Zhang R, Panwisawas C, Xia M, Dong H, Li J (2023) Solute trapping and non-equilibrium microstructure during rapid solidification of additive manufacturing. Nat Commun 14:7990. https://doi.org/10.1038/s41467-023-43563-x
21. Guo Y, Su H, Yang P, Shen Z, Zhao D, Zhao Y, Liu Y, Zhou H (2022) New insight into tailorable eutectic high entropy alloys with remarkable strength-ductility synergy and ample shaping freedom fabricated using laser powder bed fusion. Addit Manuf. https://doi.org/10.1016/j.addma.2022.103257
22. Liu Q, Ren C, Song Z, Dan X, Ju J, Yang T, Ni S, Lu J, Liu L, Pan J, Chen Z (2024) High-strength and high-conductivity additively manufactured cu-O alloy enabled by cellular microstructure. Addit Manuf 88:104244. https://doi.org/10.1016/j.addma.2024.104244
23. Makin VS, Pestov YI, Privalov VE (2013) Controllable grain-boundary displacement during recrystallization and the microrelief of a titanium surface induced by laser radiation pulses. J Opt Technol 80:91–95. https://doi.org/10.1364/JOT.80.000091
24. Roy I, Ray PK, Balasubramanian G (2022) Modeling oxidation of alcocrfeni high-entropy alloy using stochastic cellular automata. Entropy 24:1263. https://doi.org/10.3390/e24091263
25. Jiang H, Li L, Wang J, Wei C, Zhang Q, Su C, Sui H (2023) Wear properties of spark plasma-sintered AlCoCrFeNi2.1 eutectic high entropy alloy with NbC additions. Acta Metall. Sin. (Engl. Lett.) 36:987–998. https://doi.org/10.1007/s40195-023-01529-4
26. Teng J, Gong X, Yang B, Yu S, Liu J, Li Y (2021) Influence of Ti addition on oxidation behavior of ni-cr-W-based superalloys. Corros Sci 193:109882. https://doi.org/10.1016/j.corsci.2021.109882
27. Liang M, Zhang J, Gao J, Yi H, Yin B, Yang Z, Qi F, Yang Y (2025) Enhancing the oxidation resistance of AlCoCrNi high-entropy alloy via ti-induced microstructural modifications. Corros Sci 246:112746. https://doi.org/10.1016/j.corsci.2025.112746
28. Ham G-S, Kim Y-K, Na YS, Lee K-A (2020) Effect of Ti addition on the microstructure and high-temperature oxidation property of alcocrfeni high-entropy alloy. Met Mater Int 27:156–165. https://doi.org/10.1007/s12540-020-00708-7
29. Singh P, Johnson DD (2021) Designing order–disorder transformation in high-entropy ferritic steels. J Mater Res 37:136–144. https://doi.org/10.1557/s43578-021-00336-w
30. Sun Y, Gu D, Dai D, Guo M, Ge Q, Shi X, Li Y, Le G, Yao M (2020) Thermal behavior and microstructure evolution mechanism of W-20%Fe alloy fabricated by laser metal deposition. Int J Mech Sci 183:105772. https://doi.org/10.1016/j.ijmecsci.2020.105772
31. Zhang D, Qiu D, Gibson MA, Zheng Y, Fraser HL, StJohn DH, Easton MA (2019) Additive manufacturing of ultrafine-grained high-strength titanium alloys. Nature 576:91–95. https://doi.org/10.1038/s41586-019-1783-1
32. Sun Y, Gao R, Chen R, Li K, Ren C, Cheung CF, Chen Z, Wang C (2025) Deciphering the intrinsic material properties on milling mechanisms of ti-modified AlCoCrFeNi2.1 high-entropy alloy. Mater Sci Eng A 941:148634. https://doi.org/10.1016/j.msea.2025.148634
33. Yoshida S, Bhattacharjee T, Bai Y, Tsuji N (2017) Friction stress and hall-petch relationship in CoCrNi equi-atomic medium entropy alloy processed by severe plastic deformation and subsequent annealing. Scr Mater 134:33–36. https://doi.org/10.1016/j.scriptamat.2017.02.042
34. Qin M, Shivakumar S, Luo J (2023) Refractory high-entropy nanoalloys with exceptional high-temperature stability and enhanced sinterability. J Mater Sci 58:8548–8562. https://doi.org/10.1007/s10853-023-08535-y
35. Jin H, Elfimov I, Militzer M (2014) Study of the interaction of solutes with Σ5 (013) tilt grain boundaries in iron using density-functional theory. J Appl Phys 115:093506. https://doi.org/10.1063/1.4867400
36. Guo R, Yu L, Liu Z, Pan J, Yao Y, Liu L (2021) Enthalpy induced phase partition toward hierarchical, nanostructured high-entropy alloys. Nano Res 15:4893–4901. https://doi.org/10.1007/s12274-021-3912-z
37. Luan H, Huang L, Kang J, Luo B, Yang X, Li J, Han Z, Si J, Shao Y, Lu J, Yao K-F (2023) Spinodal decomposition and the pseudo-binary decomposition in high-entropy alloys. Acta Mater 248:118775. https://doi.org/10.1016/j.actamat.2023.118775
38. Chang W-C, Hsueh C-H (2023) Strengthening of CoCrNi medium entropy alloy with ti additions. Intermetallics 163:108072. https://doi.org/10.1016/j.intermet.2023.108072
39. Gao L, Wu Y, An N, Chen J, Liu X, Bai R, Hui X (2024) Nanoscale L12 phase precipitation induced superb ambient and high temperature mechanical properties in Ni–Co–Cr–Al system high-entropy superalloys. Mater Sci Eng A 898:145995. https://doi.org/10.1016/j.msea.2023.145995
40. Curry JF, Babuska TF, Furnish TA, Lu P, Adams DP, Kustas AB, Nation BL, Dugger MT, Chandross M, Clark BG, Boyce BL, Schuh CA, Argibay N (2018) Achieving ultralow wear with stable nanocrystalline metals. Adv Mater 30:1802026. https://doi.org/10.1002/adma.201802026
41. Dai Q, Xie B, Ren S, Yu Z, Xu B, Sun M (2023) Divergent interfacial behaviors of homo-/hetero-phase boundaries in a dual-phase eutectic high-entropy alloy. Sci China Mater 66:2454–2466. https://doi.org/10.1007/s40843-022-2361-4
42. Zhu Y, Ameyama K, Anderson PM, Beyerlein IJ, Gao H, Kim HS, Lavernia E, Mathaudhu S, Mughrabi H, Ritchie RO, Tsuji N, Zhang X, Wu X (2021) Heterostructured materials: superior properties from hetero-zone interaction. Mater Res Lett 9:1–31. https://doi.org/10.1080/21663831.2020.1796836
43. Liu CT, Fu CL, Chisholm MF, Thompson JR, Krcmar M, Wang X-L (2007) Magnetism and solid solution effects in NiAl (40% al) alloys. Prog Mater Sci 52:352–370. https://doi.org/10.1016/j.pmatsci.2006.10.014
44. Clausen CM, Pedersen JK, Batchelor TAA, Rossmeisl J (2021) Lattice distortion releasing local surface strain on high-entropy alloys. Nano Res 15:4775–4779. https://doi.org/10.1007/s12274-021-3544-3
45. Divinski SV, Stloukal I, Král L, Herzig C (2009) Diffusion of titanium and nickel in B2 NiTi. Defect Diffus Forum 289:377–382. https://doi.org/10.4028/www.scientific.net/DDF.289-292.377
46. Shahmir H, Mehranpour MS, Derakhshandeh A, Nili-Ahmadabadi M (2021) Microstructure tailoring to enhance mechanical properties in CoCrFeNiMn high-entropy alloy by ti addition and thermomechanical treatment. Mater Charact 182:111513. https://doi.org/10.1016/j.matchar.2021.111513
47. Kim J, Hong SJ, Lee JK, Kim KB, Lee JH, Han J, Lee C, Song G (2021) Development of coherent-precipitate-hardened high-entropy alloys with hierarchical NiAl/Ni2TiAl precipitates in CrMnFeCoNiAlxTiy alloys. Mater Sci Eng A 823:141763. https://doi.org/10.1016/j.msea.2021.141763
48. Raghavan V (1987) Solid state phase transformations. PHI Learning Pvt. Ltd.

49. Odetola PI, Babalola BJ, Afolabi AE, Anamu US, Olorundaisi E, Umba MC, Phahlane T, Ayodele OO, Olubambi PA (2024) Exploring high entropy alloys: a review on thermodynamic design and computational modeling strategies for advanced materials applications. Heliyon 10:e39660. https://doi.org/10.1016/j.heliyon.2024.e39660
50. Han C, Fang Q, Shi Y, Tor SB, Chua CK, Zhou K (2020) Recent advances on high-entropy alloys for 3D printing. Adv Mater 32:1903855. https://doi.org/10.1002/adma.201903855
51. Cantwell PR, Tang M, Dillon SJ, Luo J, Rohrer GS, Harmer MP (2014) Grain boundary complexions. Acta Mater 62:1–48. https://doi.org/10.1016/j.actamat.2013.07.037
52. Krauss G (1999) Martensite in steel: strength and structure. Mater Sci Eng A 273–275:40–57. https://doi.org/10.1016/S0921-5093(99)00288-9
53. Guo R, Zhang P, Pan J, Xu J, Liu L, Zhang C, Liu L (2024) Achieving prominent high-temperature mechanical properties in a dual-phase high-entropy alloy: a synergy of deformation-induced twinning and martensite transformation. Acta Mater 264:119591. https://doi.org/10.1016/j.actamat.2023.119591
54. Liu M, Zhang XM, Liu L, Li YY, Shelyakov AV (2000) In situ TEM observations of martensite-austenite transformations in a Ni49Ti36Hf15 high temperature shape memory alloy. J Mater Sci Lett 19:1383–1386. https://doi.org/10.1023/A:1006717619342
55. Rashad M, Rüsing M, Berth G, Lischka K, Pawlis A (2013) CuO and Co3O4 nanoparticles: synthesis, characterizations, and raman spectroscopy. J Nanomater 2013:714853. https://doi.org/10.1155/2013/714853
56. Thomas PV, Ramakrishnan V, Vaidyan VK (1989) Oxidation studies of aluminum thin films by Raman spectroscopy. Thin Solid Films 170:35–40. https://doi.org/10.1016/0040-6090(89)90619-6
57. Monnereau O, Tortet L, Grigorescu CEA, Savastru D, Iordanescu CR, Guinneton F, Notonier R, Tonetto A, Zhang T, Mihailescu IN, Stanoi D, Trodahl HJ (2010) Chromium oxides mixtures in PLD films investigated by Raman spectroscopy. J Optoelectron Adv M 12:1752–1758
58. Lee N, Schuck PJ, Nico PS, Gilbert B (2015) Surface enhanced Raman spectroscopy of organic molecules on magnetite (Fe3O4) nanoparticles. J Phys Chem Lett 6:970–974. https://doi.org/10.1021/acs.jpclett.5b00036
59. Mironova-Ulmane N, Kuzmin A, Steins I, Grabis J, Sildos I, Pärs M (2007) Raman scattering in nanosized nickel oxide NiO. J Phys Conf Ser 93:12039. https://doi.org/10.1088/1742-6596/93/1/012039
60. Yashima M, Lee J-H, Kakihana M, Yoshimura M (1997) Raman spectral characterization of existing phases in the Y2O3-Nb2O5 system. J Phys Chem Solids 58:1593–1597. https://doi.org/10.1016/S0022-3697(97)00098-X
61. Archard JF (1953) Contact and rubbing of flat surfaces. J Appl Phys 24:981–988. https://doi.org/10.1063/1.1721448
62. Zeng S, Chen C, Li M, Qi L, Meng Y, Zhu C, Han X, Zhang H (2023) Aluminum concentration effect on the oxidation behavior of CrAl coatings investigated by high-throughput method. Corros Sci 221:111327. https://doi.org/10.1016/j.corsci.2023.111327
63. Chyrkin A, Fazi A, Sattari M, Mayweg D, Thuvander M, Stiller K, Halvarsson M, Nowak WJ, Wessel E, Naumenko D, Froitzheim J (2025) Oxidation of additively manufactured ni-base alloy IN625: mechanism of intergranular oxidation. Corros Sci 256:113218. https://doi.org/10.1016/j.corsci.2025.113218
64. Zhao Z, Wang J, Chen M, Zhang J, Wang F, Young DJ (2022) Comparative study on the initial oxidation behavior of conventional and nanocrystalline MCrAlY coatings - effect of microstructure evolution and dynamic mechanisms. Acta Mater 239:118264. https://doi.org/10.1016/j.actamat.2022.118264
65. Zhang W-T, Wang X-Q, Zhang F-Q, Cui X-Y, Fan B-B, Guo J-M, Guo Z-M, Huang R, Huang W, Li X-B, Li M-R, Ma Y, Shen Z-H, Sun Y-G, Wang D-Z, Wang F-Y, Wang L-Q, Wang N, Wang T-L, Wang W, Wang X-Y, Wang Y-H, Yu F-J, Yin Y-Z, Zhang L-K, Zhang Y, Zhang J-Y, Zhao Q, Zhao Y-P, Zhu X-D, Sohail Y, Chen Y-N, Feng T, Gao Q-L, He H-Y, Huang Y-J, Jiao Z-B, Ji H, Jiang Y, Li Q, Li X-M, Liao W-B, Lin H-J, Liu H, Liu Q, Liu Q-F, Liu W-D, Liu X-J, Lu Y, Lu Y-P, Ma W, Miao X-F, Pan J, Wang Q, Wu H-H, Wu Y, Yang T, Yang W-M, Yu Q, Zhang J-Y, Chen Z-G, Mao L, Ren Y, Shen B-L, Wang X-L, Jia Z, Zhu H, Wu Z-D, Lan S (2024) Frontiers in high entropy alloys and high entropy functional materials. Rare Met 43:4639–4776. https://doi.org/10.1007/s12598-024-02852-0
66. Gupta AK, Choudhari A, Rane A, Tiwari A, Sharma P, Gupta A, Sapale P, Tirumala RTA, Muthaiah R, Kumar A (2024) Advances in nickel-containing high-entropy alloys: from fundamentals to additive manufacturing. Materials 17:3826. https://doi.org/10.3390/ma17153826
67. Huang X, Bosonnet S, Fossati PCM, Latu-Romain L, Wouters Y, Aléon J, Verdier-Paoletti M, Jomard F, Martinelli L (2025) Growth mechanism of chromia scales on a model ni-30Cr alloy at high temperatures. Corros Sci 243:112585. https://doi.org/10.1016/j.corsci.2024.112585
68. Birks N, Meier GH, Pettit FS (2006) Introduction to the high temperature oxidation of metals, 2nd edn. Cambridge University Press. https://doi.org/10.1017/CBO9781139163903
69. Wang J, Mao S, Zhang J, Young DJ (2025) Effects of si, mn, ti and ce on oxidation of fe-cr alloys in water vapour. Npj Mater Degrad 9:90. https://doi.org/10.1038/s41529-025-00641-3
70. Nawar AM, Mansour SF, Mosaad S, Ibrahim AH (2025) Single oscillator modeling of chromium oxide-doped PMMA films and electrical properties of ITO/Cr2O3-doped PMMA/ag systems for memory technology applications. J Mater Sci Mater Electron 36:295. https://doi.org/10.1007/s10854-025-14354-5
71. Holt A, Kofstad P (1999) Electrical conductivity of Cr2O3 doped with TiO2. Solid State Ionics 117:21–25. https://doi.org/10.1016/S0167-2738(98)00244-6
72. Zhou Z, Chen X, Wu D, Zhu D, Chen J, Sun X, Li M, Cai C, Yang JC, Zhou G (2025) In situ electron microscopy: atomic-scale dynamics of metal oxidation and corrosion. Npj Mater Degrad 9:28. https://doi.org/10.1038/s41529-025-00568-9
73. Du LM, Lan LW, Zhu S, Yang HJ, Shi XH, Liaw PK, Qiao JW (2019) Effects of temperature on the tribological behavior of Al0.25CoCrFeNi high-entropy alloy. J Mater Sci Technol 35:917–925. https://doi.org/10.1016/j.jmst.2018.11.023
74. Chen M, Lan L, Shi X, Yang H, Zhang M, Qiao J (2019) The tribological properties of Al0.6CoCrFeNi high-entropy alloy with the σ phase precipitation at elevated temperature. J Alloys Compd 777:180–189. https://doi.org/10.1016/j.jallcom.2018.10.393
75. Geng Y, Zhang J, Wang H, Chen J, Gong H, Yang D, Cheng J, Yang Y, Yang J, Liu W (2025) Ultra-wear-resistant high-entropy nanocomposite through gradient nanograined glaze-layer at 1000°C. Compos B-Eng 299:112419. https://doi.org/10.1016/j.compositesb.2025.112419
76. Zhang Y-Y, Yang C-R, Tong X, Zhou J, Liu L, Xiao M, Ke H-B, Chan K-C, Wang W-H (2025) Oxidation sequence modulation induced superior high-temperature tribological performance of ti-hf-nb-V refractory high entropy alloy fabricated through directed energy deposition. Rare Met 44:2695–2704. https://doi.org/10.1007/s12598-024-03153-2
77. Yang H, Liu Y, Zhang T, Wang H, Tang B, Qiao J (2014) Dry sliding tribological properties of a dendrite-reinforced zr-based bulk metallic glass matrix composite. J Mater Sci Technol 30:576–583. https://doi.org/10.1016/j.jmst.2014.05.004
78. Huang L, Han Y, Sun Y, Pattamatta ASLS, Luan J, Wang Q, Ren C, Zhou Y, Li J, Luan H, Liaw PK, Lu J (2025) Vermicular eutectic multi-principal element alloy with exceptional strength and ductility. Adv Sci 2501150. https://doi.org/10.1002/advs.202501150